



Publication Year	2019
Acceptance in OA @INAF	2021-04-13T11:26:16Z
Title	A Global Inventory of Ice-Related Morphological Features on Dwarf Planet Ceres: Implications for the Evolution and Current State of the Cryosphere
Authors	Sizemore, H. G.; Schmidt, B. E.; Buczkowski, D. A.; Sori, M. M.; Castillo-Rogez, J. C.; et al.
DOI	10.1029/2018JE005699
Handle	http://hdl.handle.net/20.500.12386/30747
Journal	JOURNAL OF GEOPHYSICAL RESEARCH (PLANETS)
Number	124

JGR Planets

RESEARCH ARTICLE

10.1029/2018JE005699

Special Section:

Ice on Ceres

Key Points:

- We present a global catalog and maps of the morphological features relevant to subsurface ice identified during the Dawn mission at Ceres
- Morphology suggests ice concentration is heterogeneous in the upper kilometers of Ceres' crust; impacts likely contribute to heterogeneity
- We highlight locations where future analysis may provide insights into putative cryovolcanic features and current H₂O loss mechanisms

Supporting Information:

- Supporting Information S1
- Data Set S1

Correspondence to:

H. G. Sizemore,
sizemore@psi.edu

Citation:

Sizemore, H. G., Schmidt, B. E., Buczkowski, D. A., Sori, M. M., Castillo-Rogez, J. C., Berman, D. C., et al. (2019). A global inventory of ice-related morphological features on dwarf planet Ceres: Implications for the evolution and current state of the cryosphere. *Journal of Geophysical Research: Planets*, 124, 1650–1689. <https://doi.org/10.1029/2018JE005699>

Received 20 MAY 2018

Accepted 4 DEC 2018

Accepted article online 11 DEC 2018

Published online 2 JUL 2019

Author Contributions:

























Conceptualization: B. E. Schmidt, J. C. Castillo-Rogez, C. T. Russell, C. A. Raymond

Data curation: B. E. Schmidt, D. A. Buczkowski, M. M. Sori, K. H. G. Hughson, K. Duarte, K. A. Otto, M. T. Bland, A. Neesemann, J. E. C. Scully, D. A. Crown, P. Schenk

Formal analysis: B. E. Schmidt, D. A. Buczkowski, M. M. Sori, J. C. Castillo-Rogez, K. H. G. Hughson, K. Duarte, D. A. Otto, M. T. Bland, A. Neesemann, J. (continued)

©2018. American Geophysical Union.
All Rights Reserved.

A Global Inventory of Ice-Related Morphological Features on Dwarf Planet Ceres: Implications for the Evolution and Current State of the Cryosphere

H. G. Sizemore¹ , B. E. Schmidt² , D. A. Buczkowski³ , M. M. Sori⁴ , J. C. Castillo-Rogez⁵, D. C. Berman¹ , C. Ahrens⁶ , H. T. Chilton² , K. H. G. Hughson⁷ , K. Duarte², K. A. Otto⁸ , M. T. Bland⁹ , A. Neesemann¹⁰ , J. E. C. Scully⁵ , D. A. Crown¹ , S. C. Mest¹ , D. A. Williams¹¹ , T. Platz¹ , P. Schenk¹², M. E. Landis⁴ , S. Marchi¹³ , N. Schorghofer¹ , L. C. Quick¹⁴ , T. H. Prettyman¹ , M. C. De Sanctis¹⁵ , A. Nass⁸, G. Thangjam¹⁶, A. Nathues¹⁶, C. T. Russell⁷ , and C. A. Raymond⁵ 

¹Planetary Science Institute, Tucson, AZ, USA, ²School of Earth and Atmospheric Sciences, Georgia Institute of Technology, Atlanta, GA, USA, ³Johns Hopkins University Applied Physics Laboratory, Laurel, MD, USA, ⁴Lunar and Planetary Laboratory, University of Arizona, Tucson, AZ, USA, ⁵Jet Propulsion Laboratory, California Institute of Technology, Pasadena, CA, USA, ⁶Arkansas Center for Space and Planetary Science, University of Arkansas, Fayetteville, AR, USA, ⁷University of California, Los Angeles, Los Angeles, CA, USA, ⁸German Aerospace Center, Institute of Planetary Research, Berlin, Germany, ⁹USGS Astrogeology, Flagstaff, AZ, USA, ¹⁰Institute of Geological Sciences, Freie Universität Berlin, Berlin, Germany, ¹¹School of Earth and Space Exploration, Arizona State University, Tempe, AZ, USA, ¹²Lunar and Planetary Institute, Houston, TX, USA, ¹³Southwest Research Institute, Boulder, CO, USA, ¹⁴Center for Earth and Planetary Studies, Smithsonian Institution, Washington, DC, USA, ¹⁵Istituto di Astrofisica e Planetologia Spaziali, INAF, Rome, Italy, ¹⁶Max Planck Institute for Solar System Research, Göttingen, Germany

Abstract We present a comprehensive global catalog of the geomorphological features with clear or potential relevance to subsurface ice identified during the Dawn spacecraft's primary and first extended missions at Ceres. We define eight broad feature classes and describe analyses supporting their genetic links to subsurface ice. These classes include *relaxed craters*; *central pit craters*; *large domes*; *small mounds*; *lobate landslides and ejecta*; *pitted materials*; *depressions and scarps*; and *fractures, grooves, and channels*. Features in all classes are widely distributed on the dwarf planet, consistent with multiple lines of observational evidence that ice is a key component of Ceres' crust. Independent analyses of multiple feature types suggest rheological and compositional layering may be common in the upper ~10 km of the crust. Clustering of features indicates that ice concentration is heterogeneous on nearly all length scales, from ~1 km to hundreds of kilometers. Impacts are likely the key driver of heterogeneity, causing progressive devolatilization of the low latitude and midlatitude crust on billion-year timescales but also producing localized enhancements in near surface ice content via excavation of deep ice-rich material and possible facilitation of cryomagmatic and cryovolcanic activity. Impacts and landslides may be the dominant mechanism for ice loss on modern Ceres. Our analysis suggests specific locations where future high-resolution imaging can be used to probe (1) current volatile loss rates and (2) the history of putative cryomagmatic and cryovolcanic features. The Cerean cryosphere and its unique morphology promise to be a rich subject of ongoing research for years to come.

Plain language summary Planetary scientists are interested in understanding where ice is located in the solar system for two reasons. First, water is necessary to sustain life as we know it, so extraterrestrial ice may provide habitats for past or present life. Second, water ice can be used to produce rocket fuel; in the future, ice may be mined from asteroids, moons, and planets to fuel spacecraft carrying humans. Ceres has been predicted to contain large amounts of ice for decades. When the Dawn spacecraft arrived at Ceres, a major goal for the science team was confirming the presence of ice and understanding how it is distributed beneath the surface. One aspect of that investigation was identifying landforms (features like mountains or craters on the surface) whose appearance indicates the presence of ice. In this study, we compiled a catalog and global maps of all of the "icy" landforms identified during Dawn's primary mission at Ceres. We used these maps, together with detailed analysis of each type of landform, to develop a global picture of how ice is distributed in Ceres' crust. We found that the concentration of ice was spatially variable and that layering of icy and less icy materials may be common. We also identified specific areas of Ceres that may be particularly ice-rich, so that future missions can target these areas for more analysis.

E. C. Scully, P. Schenk, M. E. Landis, A. Nathues

Investigation: B. E. Schmidt, D. A. Buczkowski, C. Ahrens, K. H. G. Hughson, K. Duarte, K. A. Otto, M. T. Bland, T. Platz, P. Schenk, G. Thangjam, A. Nathues

Methodology: D. A. Buczkowski, M. M. Sori, D. C. Berman, M. T. Bland, D. A. Williams, A. Nass

Resources: B. E. Schmidt, S. C. Mest

Validation: B. E. Schmidt, D. A. Buczkowski, M. M. Sori, H. T. Chilton, K. H. G. Hughson, K. Duarte, K. A. Otto, M. T. Bland, A. Neesemann, J. E. C. Scully, D. A. Crown, S. C. Mest, T. Platz, P. Schenk, M. E. Landis, S. Marchi, N. Schorghofer, L. C. Quick, T. H. Prettyman, M. C. De Sanctis, G. Thangjam, A. Nathues

Visualization: D. A. Buczkowski, C. Ahrens

Writing - original draft: M. M. Sori, J. C. Castillo-Rogez

Writing - review & editing: B. E. Schmidt, D. A. Buczkowski, M. M. Sori, J. C. Castillo-Rogez, D. C. Berman, C. Ahrens, K. H. G. Hughson, K. Duarte, K. A. Otto, M. T. Bland, J. E. C. Scully, D. A. Crown, S. C. Mest, D. A. Williams, M. E. Landis, S. Marchi, N. Schorghofer, L. C. Quick, T. H. Prettyman, M. C. De Sanctis, A. Nathues, C. T. Russell

1. Introduction

Understanding the geographic distribution, burial depth, concentration, and mobility of subsurface water ice on inner solar system worlds is of great interest from the standpoints of cosmochemistry, astrobiology, and future in situ resource utilization. Dwarf planet Ceres is the most water rich large body in the inner solar system in terms of relative mass fraction (~25 wt. %). Data sets collected by the Dawn spacecraft during its primary mission at Ceres have confirmed the presence of substantial subsurface ice and revealed a more complex distribution of ice than was previously predicted (Bland et al., 2016; Combe et al., 2018; Fu et al., 2017; Prettyman et al., 2017). The inventory of ice in localized surface exposures on Ceres has been quantified by the Visible and InfraRed Mapping Spectrometer (VIR; Combe et al., 2016, 2018; Platz et al., 2016). The ice content of the uppermost meter of Ceres' regolith is well characterized by data from Dawn's Gamma Ray and Neutron Detector (GRaND; Prettyman et al., 2017) and by thermal stability simulations (Schorghofer, 2016). The ice content of the deep interior (length scales of tens of kilometers) is constrained by gravity and global topography data (Ermakov, Fu, et al., 2017; Fu et al., 2017). At intermediate depth ranges (tens of meters to kilometers), analysis of surface morphology has been critical to investigating the concentration of ice and other volatiles (Bland et al., 2016; Schenk et al., 2015; Schmidt et al., 2017; Sizemore et al., 2017). Here we present a comprehensive catalog of morphological features relevant to the presence and concentration of subsurface ice and water-rich phases on Ceres, along with updated global maps of features that have been previously studied. We discuss the implications for local and regional variations in subsurface ice content and the long-term evolution of the Cerean cryosphere.

2. Background and Methods

2.1. Pre-Dawn Expectations and Search Criteria Development

Theoretical predictions of Ceres' interior layer structure (Castillo-Rogez & McCord, 2010; McCord & Sotin, 2005) and of the burial depth of shallow ice (Fanale & Salvail, 1989; Schorghofer, 2008) were in place at the outset of the Dawn mission. Based on these predictions, we expected Ceres' surface morphology to have characteristics in common with Mars, solid airless bodies (Mercury and the Moon), and the icy satellites of the outer solar system. We compiled lists of features observed on specific solar system bodies that might be relevant to subsurface ice on Ceres, then we developed broad search criteria for identifying similar classes of features during the active mission. We describe the framework in which we made predictions in this section, and we discuss the development of search criteria in sections 2.1.1 through 2.1.4.

In the very shallow subsurface (<1 km), the distribution of ice burial depths on Ceres was predicted to be directly analogous to the Martian cryosphere. On Mars, under current climate conditions, ground ice is thermally stable at depths of a meter or less at latitudes higher than ~50° in both hemispheres, with burial depth decreasing toward the poles, where surface ice becomes stable (e.g., Boynton et al., 2002; Mellon et al., 2008; Prettyman et al., 2004). Similarly, on Ceres, ice was predicted to be present at depths of tens to hundreds of meters at the equator, with burial depths decreasing toward the poles, where ice could be protected from sublimation by only centimeters or millimeters of dry silicate regolith and localized exposures of metastable ice might be possible. On Ceres as on Mars, ice-cemented materials were expected to be sharply delineated from a dry protective layer by a boundary termed the "ice table." Importantly, ground ice is also observed at depths <1 m on Mars at some locations where it is not thermally stable (e.g., Byrne et al., 2009); similar low-latitude, thermally unstable ice was anticipated to occur on Ceres at locations where recent geologic activity delivered materials to the near surface from depth.

Similarities with Mars, particularly the intimate mixing of ice and silicates in the upper hundreds of meters, led us to anticipate several specific types of features that might be observed on Ceres. These features included (1) layered ejecta, (2) lobate landslide features with characteristics of rock glaciers, (3) pits, scarps, and dissected terrains indicative of sublimation, (4) polygonal terrains associated with thermal contraction, and (5) pingos. The lack of a substantial atmosphere on Ceres also led to important differences predicted for Ceres, such as the absence of extensive surface polar ice deposits and the absence of landforms related to CO₂ ice.

Based on simulations of Ceres' thermal evolution, Castillo-Rogez and McCord (2010) predicted that the dwarf planet's deep interior (kilometer to ~100 km) was similar to small icy satellites, with an icy crust overlying a rocky mantle and the possibility of a relict brine layer (or brine pockets) persisting into the geologically recent past. Neveu and Desch (2015) separately predicted that Ceres might contain a remnant muddy layer at the interface between the icy crust and mantle. Both of these studies suggested that diapirism or cryovolcanism may have occurred on Ceres, leading us to predict that the occurrence of domical or conical mountains could provide morphological evidence of interior activity at the surface. The detection of water vapor outgassing from Ceres while Dawn was en route lent some support to our prediction, as cryovolcanism was one of the mechanisms hypothesized to explain active outgassing (Küppers et al., 2014). (Small impacts and an enhanced sublimation process were also hypothesized.) Predicted similarities between Ceres and the icy satellites also suggested to us that large-scale crater morphology could be an indicator of subsurface ice content at multikilometer length scales (Bland, 2013).

2.1.1. Search Criteria: Characteristics of Craters

Pre-Dawn-arrival analysis of impact cratering on Ceres (Schenk et al., 2016) predicted that craters in the 10- to 300-km size range would have large conical central peaks, based on the prevalent crater morphology observed on similarly sized ice-rich Dione and Tethys (e.g., White et al., 2013, 2017). Transition diameters from simple to complex craters scale inversely with surface gravity of the host planetary body throughout the solar system. Pre-Dawn-arrival analysis suggested that the simple-to-complex transition diameter on Ceres would follow the same trend as other icy bodies (i.e., the Galilean and Saturnian satellites) and be clearly distinct from the trend for rocky bodies (the Moon, Mars, Mercury, and Vesta).

The expectation that Ceres' crust would consist of a mixture of ice and silicates in unknown proportions suggested a range of possible crater morphologies. In particular, Dombard and Schenk (2013) and Bland (2013) both used finite element simulations of crater relaxation to predict that a Cerean crust volumetrically dominated by ice to depths of a kilometer to tens of kilometers would cause rapid crater relaxation near Ceres' equator and produce strong latitudinal trends in crater density. Bland (2013) also predicted that a silicate-dominated shell would produce negligible crater relaxation. This analysis suggested details of subsurface stratigraphy could be inferred from comparisons of large-scale crater morphology to relaxation models, and that more generally, very shallow impact structures and regional deficits in crater density would be indicators of high ice content.

The expectation of a mixed ice-silicate target material also led us to predict the production of craters with layered ejecta, analogous to craters observed on Mars and Ganymede with distinctive, high-standing lobate margins and evidence of postdepositional flow (Barlow et al., 2000). Similarly, analogies with Mars suggested mass wasting features with characteristics of terrestrial and Martian rock glaciers (i.e., steep-toed, lobate margins, and streamlined furrows) might occur at locations where impact heating produced temperatures high enough to allow for ductile creep. Thus, we searched for lobate features with evidence for flow or creep, inside and outside of craters, as well as abnormally shallow impact structures.

2.1.2. Search Criteria: Mountains and Hills

Prior to Dawn's arrival at Ceres, two lines of reasoning suggested that Ceres might host distinct domical to conical hills and mountains linked to upwelling of ice-rich material. First, the predictions of an icy outer shell and possible persistent brine layers or inclusions (Castillo-Rogez & McCord, 2010) suggested analogies with icy outer solar system worlds and the possibility of cryovolcanism (Kargel, 1991). On Europa, a variety of multikilometer scale domes have been observed and attributed variously to melting, intrusion, diapirism, and cryovolcanic extrusion (Culha & Manga, 2016; Fagents, 2003; Pappalardo et al., 1999; Pappalardo & Barr, 2004; Quick et al., 2017; Schmidt et al., 2011). Similarly, hills and mounds in the Sotra region of Titan have been hypothesized to be cryovolcanic (Lopes et al., 2013) or arise from other endogenic activity. The European and Titanian features suggested that the occurrence of domes, mounds, or cones with diameters of kilometer to tens of kilometers and relief of hundreds of meters to kilometers might indicate endogenic processes if observed on Ceres.

Second, the expectation that Ceres' outermost shell would consist of an intimate mixture of ice and silicates suggested to us that periglacial morphology observed on Earth and Mars might occur on Ceres, particularly in regions where impacts had produced transient melt and refreezing. The type of periglacial feature we thought most likely to be resolved in Framing Camera (FC) images (anticipated pixel scales >35 m per pixel) was pingos. Pingos are ice-cored hills tens to hundreds of meters in diameter that develop via cryosuction

during the progressive freezing of surface lakes or shallow-subsurface water reservoirs. Pingos are observed extensively in terrestrial permafrost regions, and candidates have been identified and vetted at a variety of locations on Mars (Dundas & McEwen, 2010).

The domes of Europa and Titan, as well as terrestrial and Martian pingos, are sometimes associated with pits or depressions of comparable scale (e.g., Dundas & McEwen, 2010; Pappalardo et al., 1998). The domes in Titan's Sotra region are associated with both craters and flows (Lopes et al., 2013). Because pits and depressions can be produced by a variety of geophysical processes (including impacts and sublimation), we considered domes to be less ambiguous markers of endogenic activity. Thus, we searched for distinct, isolated, positive topography features in the diameter range < 1 km to tens of kilometers on Ceres. We searched preferentially for features that were round in planform, with domical or conical elevation profiles. We did not establish a priori criteria for the presence of pits, flows, embayment relationships, or fractures in our identification of positive topography features.

2.1.3. Search Criteria: Sublimation Terrains

Sublimation of surface and subsurface ices is a solar system wide process that influences the morphology of multiple planetary bodies (Mangold, 2011; Moore et al., 1996), including Mercury, Earth, Mars, Callisto, Ganymede, Europa, Iapetus, and Pluto (Blewett et al., 2011; Giese et al., 2008; Marchant et al., 2002; Milliken & Mustard, 2003; Moore et al., 2016; Soderblom, Kreidler, & Masursky, 1973). Ceres was expected to exhibit morphology linked to sublimation, based on observations of pits, depressions, and scarps on a variety of airless solar system bodies and Mars. On airless bodies, morphology linked to sublimation can occur at local (Mercury), regional (Ganymede), and near-global scales (Callisto). Early simulations of ice sublimation in the asteroid belt (Fanale & Salvail, 1989; Schorghofer, 2008) predicted that the distribution of ice burial depths on Ceres would be analogous to Mars and further predicted that thin transient surface ice deposits might occur near Ceres' poles. Together, these predictions suggested to us that pitted and dissected terrains might occur extensively on Ceres and, moreover, that the scale and morphology of pits and scarps might depend strongly on latitude. On Mars, sublimation pits and scarps occur at spatial scales ranging from hundreds of kilometers (Soderblom, Kreidler, & Masursky, 1973) to meters (Schon et al., 2009; Searls et al., 2007). Martian polar landscapes dominated by ice loss were first recognized in Mariner 7 and Mariner 9 images (Cutts et al., 1971; Sharp et al., 1971; Soderblom, Malin, et al., 1973). Subsequent higher-resolution imaging by the Viking Orbiters, Mars Global Surveyor, Mars Odyssey, Mars Reconnaissance Orbiter, and Mars Express has revealed sublimation morphology at progressively smaller spatial scales at all latitudes (e.g., Byrne & Ingersoll, 2003). By analogy, we expected the occurrence, size, style, and spatial concentration of pits and scarps to serve as potential indicators of ice concentration and burial depth on Ceres, with regional variations potentially indicating areas of enhanced or depleted ice concentration and/or resurfacing processes.

Our criteria for identification of pits, depressions, and pit clusters relevant to volatiles were the presence of (1) rimless depressions, with (2) round-to-irregular, elongate, branching, or polygonal margins, and exhibiting (3) overlapping or repeating patterns (Sizemore et al., 2017). We based these criteria primarily on characteristics of the Martian "Swiss Cheese" and dissected mantle terrains (Malin et al., 2001; Milliken & Mustard, 2003), the morphology of pitted materials inferred to be volatile rich in craters on Vesta, Mars, and Mercury (Blewett et al., 2011; Denevi et al., 2012; Tornabene et al., 2012), and reviews of ice sublimation as a geomorphic process (Mangold, 2011; Moore et al., 1996). These criteria explicitly include features produced by long-term sublimation of ices at local average temperatures, as well as features produced by rapid, high-temperature outgassing as a result of impact heating.

2.1.4. Search Criteria: Polygonal Patterned Ground

Thermal contraction polygons are a class of small-scale periglacial features that occur on both Earth and Mars due to repeated seasonal cooling and contraction of ice-cemented soils. Cracks form in ice-rich ground when tensile stresses caused by dropping temperatures exceed the tensile strength of the ice-rich soil matrix. Once formed, a crack may fill with surface melt water (on Earth), or soil/regolith (on Earth and Mars), leading to a progressive widening and deepening of the stress-relieving fracture by an ice or soil wedge. Typically, many intersecting cracks form, producing a honeycomb network of fractures horizontally spaced at distances of a few to hundreds of meters and penetrating to depths of several meters (Mangold, 2005; Mellon et al., 1997). The resulting hummocky patterned ground is often made more distinct by preferential sublimation of ice at troughs associated with cracks and/or by preferential accumulation of boulders in troughs and trough intersections.

On Ceres, equatorial temperatures are comparable to temperatures at the Martian poles, and polar temperatures are ~50 K lower. Colder temperatures produce a more brittle ice-silicate matrix, generally favoring polygon formation (Mellon et al., 1997). However, Ceres' year is about 2.5 times longer than the Martian year, and the dwarf planet's low obliquity produces low amplitude seasonal temperature oscillations (<20 °C at Ceres' subsolar point, compared to ~35 °C on Mars), which can allow stresses to dissipate, allowing fractures to occur at wider spacings or preventing their formation entirely. Thus, if polygons form on Ceres, their characteristic length scale could be larger than on Mars, where the more rapid seasonal buildup of stresses forces polygons to subdivide.

We considered the detection of polygons on Ceres to be somewhat unlikely, because only the largest Martian features (~300-m diameter) could be resolved in FC images and because any Cerean polygons should preferentially occur at high latitudes, where ground ice was predicted to be shallowly buried, but lighting conditions are not favorable for detection of marginally resolved features. Nonetheless, we searched for groups of polygonal features <1 km in diameter *and* surface textures analogous to Martian "basketball" terrains, which provided the first indication of extensive polygons in the Martian high latitudes from low resolution images (Mustard et al., 2001).

2.2. Search Procedures

We carried out systematic global searches for features of interest (section 2.1) in individual FC images and global and regional mosaics during each of Dawn's mapping orbits at Ceres, beginning with Rotational Characterization 3 (RC3; 1.3 km per pixel), and continuing through Survey (410 m per pixel), High Altitude Mapping Orbit (HAMO; 140 m per pixel), and Low Altitude Mapping Orbit (LAMO; 35 m per pixel). As each global data set became available, it was searched independently, then features identified in previous, lower resolution data sets were reevaluated and interpreted based on the highest resolution images and digital terrain models. Although pre-Dawn-arrival predictions guided our searches, we identified and mapped some features that had clear relevance to water ice that we had not specifically anticipated. We grouped identified landforms into descriptive feature classes and evaluated their relevance to ice based on morphological comparisons to features identified elsewhere in the solar system, geological setting, compositional constraints from VIR, GRaND, and gravity data, and numerical modeling. This effort took place in parallel with the LAMO-based quadrangle mapping effort (D. A. Williams et al., 2017) and utilized the ArcGIS software package. The final list of included feature classes was informed by collaborative decisions made in the production of the geologic maps. Our final catalog and feature maps include both (1) features for which there is substantial evidence that ice played a key role in landscape development and (2) features for which there is a circumstantial case for ice or volatile involvement and which merit further scrutiny in the event of a future Ceres mission. Here we describe the defining characteristics, classification, and global distribution of these features and discuss implications for local and regional variations in subsurface ice content and the evolution of the Cerean cryosphere. More detailed analysis of individual feature types is presented by Chilton et al. (2019), Duarte et al. (2019), Hughson et al. (2019), Buczkowski et al. (2018), and Otto et al. (2019).

3. Results

We identified eight broad classes of features with clear or potential relevance to ground ice: *relaxed craters* (section 3.1.1), *central pit craters* (section 3.1.2), *large domes* (section 3.2.1), *small mounds* (section 3.2.2), *lobate landslides and ejecta* (section 3.3), *pitted materials* (section 3.4), *depressions and scarps* (section 3.4), and *fractures, grooves, and channels* (section 3.5). Characteristics of these feature classes, evidence linking their formation to ice, and inferences about ice concentration and distribution that can be drawn from their analysis are described below. Some features that were predicted to occur on Ceres were not observed; their nondetection is discussed in section 3.6. Selection biases affecting the interpretation of the entire data set are discussed in section 4.3.

3.1. Large-Scale Crater Morphology

3.1.1. Relaxed Craters

We identified five large, shallow craters with morphology and depth (d) to diameter (D) ratio (d/D) consistent with relaxation of a water ice-dominated target material based on comparisons to rheological simulations of crater relaxation (Bland et al., 2016). These include Coniraya, Kunitoga, Kerwan, Omonga, and Geshtin craters, as well as an unnamed crater in the southern hemisphere (Table 1 and supporting information S1).

Table 1
Locations, Diameters, and Depths of Relaxed Craters

Crater name	Latitude	Longitude	Diameter (km)	Apparent depth (km)	Expected depth (km)
Coniraya	40	66	135	0.5	4–5 km
Geshtin	57	−101	80	2	2.5–3.5
Omonga	58	72	77	2	2.5–3.5
Kumitoga	−10	179	96	2.5	3–4
Unnamed	−29	−167	85	0.5–1	2.5–3.5
Kerwan	−11	124	280	<1–5	6–8

Note. Expected depths are based on measurements of craters of equivalent diameter on Ceres and Tethys. All depths are relative to the surrounding terrain, not crater rims.

Figure 1 shows a map of the global distribution of large relaxed craters and central pit craters (section 3.1.2). Figure 2 shows the topography of Coniraya, Kumitoga, Geshtin, and Kerwan. A number of smaller, shallow craters were observed but are not cataloged here because it is unclear if they are relaxed or heavily degraded by subsequent impacts. Geshtin crater is included in our inventory as an explicitly marginal case that illustrates this ambiguity. On average, the apparent depth of Geshtin (depth measured relative to the surrounding terrain) is ~2 km; apparent depth at some floor locations is as high as 3 km. Datan crater overprints Geshtin, and Datan ejecta may contribute up to 1 km of material to the Geshtin floor, making it unclear if relaxation or degradation by subsequent impacts and landslides (section 3.3) is the dominant factor controlling Geshtin’s morphology. Other members of the feature class are less ambiguously shallow.

Notably, all the identified relaxed craters occur in close proximity to craters of similar age with well-preserved topography, indicating strong compositional heterogeneities on vertical and lateral length scales of tens of kilometers. Kerwan crater exhibits distinctive topography in which outer portions are relaxed, but the central portion is not. Comparisons to numerical simulations of viscous relaxation of heterogeneous subsurfaces suggest this unique topography is most consistent with devolatilization of a plug of material at Kerwan’s center by the impact itself (Bland, Ermakov, et al., 2018).

The majority of Ceres’ abundant craters are not relaxed. Dramatic crater topography and a globally high crater density were apparent immediately upon Dawn’s arrival at Ceres (Buczkowski et al., 2016). Comparisons of d/D for Ceres’ largest craters to finite element simulations of viscous relaxation indicated that most had experienced negligible relaxation (Bland et al., 2016) and suggested that Ceres was less ice-rich than anticipated. At the same time, morphological analysis indicated that the transition from simple to complex craters on Ceres occurred at a d/D consistent with icy Saturnian satellites and inconsistent with rocky bodies (Hiesinger et al., 2016). Together, these two lines of analysis indicated that Ceres’ crust (roughly Ceres’ outer 40 km; Fu et al., 2017) is composed of a material that behaved like ice on short timescales/high strain rates and like rock on long timescales/low strain rates. Bland et al. (2016) concluded that an outer shell composed of <35 vol. % ice could produce the observed rheology. Later comparisons of global topography and gravity data (Ermakov, Fu, et al., 2017; Fu et al., 2017) specifically favored a three-component mixture of <25 vol. % water ice, <29% carbonates and phyllosilicates, and >36 % high strength hydrated phases, for example, clathrates and hydrated salts, which are both predicted to be present based on geochemical modeling (Castillo-Rogez et al., 2018). The unique global-scale rheology, and the likely abundance of high-strength, low-density, water-bearing phases in the crust introduces unique challenges for interpreting the role of ice in Cerean landscape development. In high temperature processes, ice, clathrate, and hydrated salts can all supply water

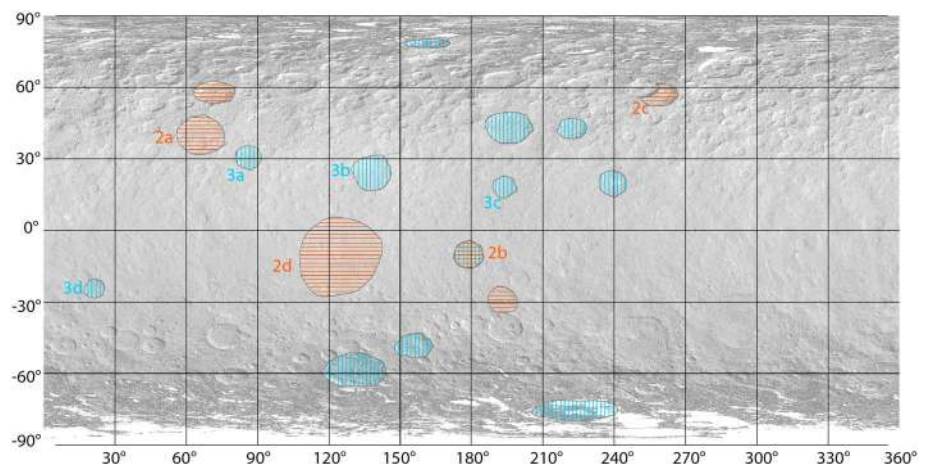


Figure 1. The global distribution of *relaxed craters* (horizontal orange hash marks) and *central pit craters* (vertical blue hash marks). The base image is the global Low Altitude Mapping Orbit mosaic (35 m per pixel) courtesy of the German Aerospace Center (DLR).

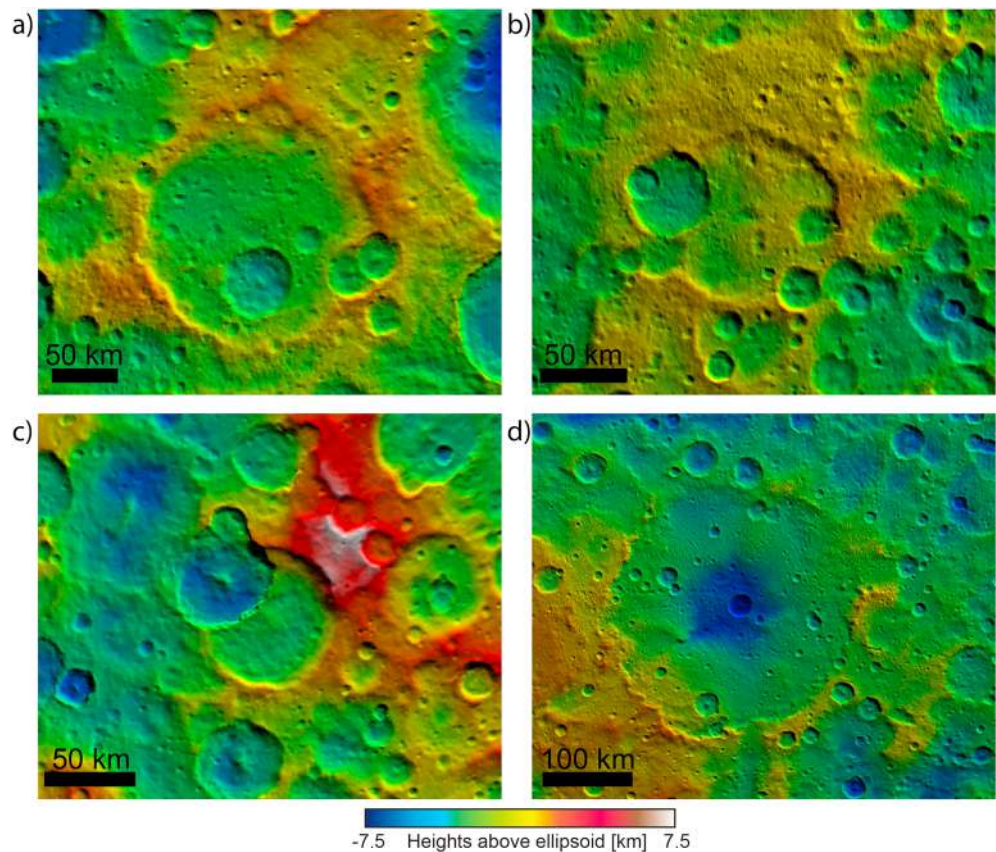


Figure 2. Examples of relaxed craters identified via comparison of topographic shape models to simulations of viscous relaxation. High Altitude Mapping Orbit colored topography (60 pixel per degree), courtesy of DLR. (a) Coniraya Crater, (b) Kunitoga Crater, (c) Geshtin Crater, and (d) Kerwan crater.

vapor or liquids that contribute to final observed morphology. At lower temperatures and on longer time-scales, the behavior of low-density high-strength materials is difficult to distinguish from the behavior of silicates. Thus, small variations in total ice content or temperature can have a dramatic effect on resultant morphology. Also, at low temperatures, there is a semantic choice to be made concerning whether clathrate hydrate falls under the broad definition of “ground ice.” On Earth, clathrates are an intrinsic component of the permafrost (Kargel & Lunine, 1998); thus, an inferred abundance of clathrates on Ceres should not be

interpreted as a deficit of ice. We revisit these themes in subsequent sections and make distinctions between conventional water ice and low-density water-bearing phases where possible. In the case of the relaxed craters mapped in Figure 1, these craters indicate locations where conventional water ice comprises >40 vol. % of the crust (Bland et al., 2016).

3.1.2. Central Pit Craters

Contrary to expectations, Cerean craters in the diameter range ~70 to 150 km commonly exhibit central depressions or pits, rather than the anticipated conical central peaks. In a global survey of well-preserved crater morphologies, ~11 out of 14 craters between 75 and 200 km across whose central structures were not obscured by postimpact modification possess partially rimmed central depressions or pits (Scully, Russell, et al., 2018). Several more degraded craters also show evidence of a central depression. We mapped 11 examples in the feature class central pit craters (Table 2, Figure 1 and supporting information S1). Occator crater is the youngest and best-preserved example in this class.

Table 2
Central Pit Craters

Name	Latitude	Longitude	Diameter (km)	Depth (km)	Central feature
Dantu	24.1	138.8	120.4	4.8	Pit
Chaminuka	-59	131	109	4.8	Pit
Kunitoga	-10	179	96		Pit
Occator	19.6	239.7	89.8	3.7	Pit
Toharu	-48.5	155	82	4.9	Pit/peak
Gaue	30.3	86	78.2	4.3	Pit
Nawish	18.2	193.8	76		Pit
Unnamed	-75	225.4	71.4		Pit/peak
Kaikara	41.8	222.2	68		Pit?
Jarimba	-24	21	67		Pit
Unnamed	78	161	28.9		Peak/pit

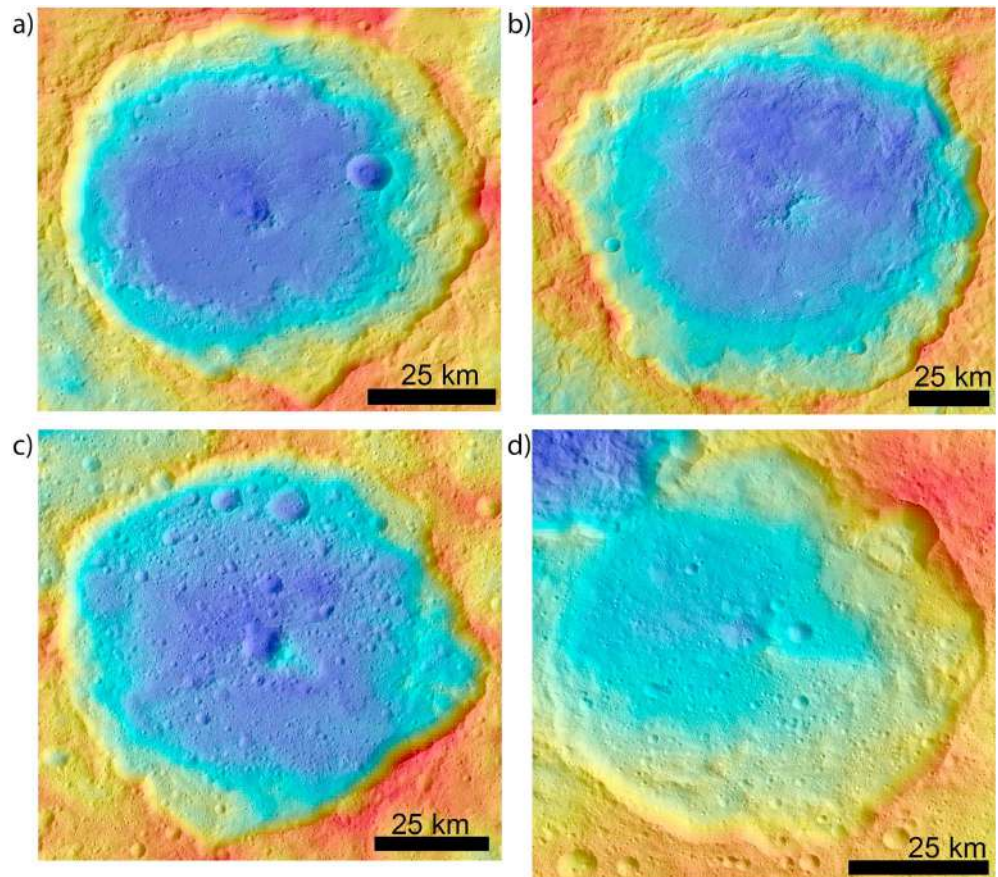


Figure 3. Examples of *central pit craters* excerpted from the global Low Altitude Mapping Orbit mosaic (35 m per pixel) overlaid with High Altitude Mapping Orbit color topography, both courtesy of DLR. (a) Gaue crater, (b) Dantu crater, (c) Nawish crater, and (d) Jarimba.

Figure 3 shows examples of central pits in Gaue, Dantu, Nawish, and Jarimba craters. Our catalog explicitly includes very well preserved, unambiguous central pits (e.g., Gaue, Figure 3a) and more degraded individual examples that might alternatively be interpreted as small impact craters on the host crater floor (e.g., Jarimba, Figure 3d). In all cataloged examples, the pit rim is asymmetric and usually incomplete (e.g., Figure 3b). The pit rim is raised above the crater floor, typically consisting of angular massifs or amphitheater enclosures. Some high-latitude examples (Toharu and Cahminuka) have steeply ramping pit walls that elevate the pit floor above the level of the crater floor. The Occator central pit is not pictured in Figure 3; it is the only central pit crater on Ceres that also possesses an interior central dome (Figure 7a and section 3.2.2). Central pit/dome complexes are common on Ganymede, so it is unclear if dome formation at Occator was a unique event on Ceres, or if central domes are fragile and have been destroyed in older Cerean craters.

The observation of central pits on Ceres was surprising, both because of the lack of comparable structures on the similarly sized Saturnian satellites and because analysis of central pit craters in the ~30–60-km range on Ganymede and Callisto had suggested that central pits could not develop on lower gravity bodies (Schenk, 1993). Central pit craters with morphologies directly analogous to the Cerean features have been observed on Ganymede and Callisto since the Voyager era (e.g., Alzate & Barlow, 2011; Passey & Shoemaker, 1982; Schenk, 1993). They are the dominant crater class in the >25-km range on both bodies, and they fall into two gradational classes: central pit and central dome craters (Schenk, 1993; Schenk et al., 2004), both of which are observed on Ceres. The observation of central pit craters on Ceres also establishes an unanticipated parallel with Mars, where central pits occur sporadically in a variety of craters (Barlow, 2006).

The formation of central pits is poorly understood. Four development models have been proposed, all of them dependent upon the availability of water or ice. The first model contends that pits are formed via a

Table 3
Large Domes

Object ID	Latitude	Longitude	IAU* name	Figure
1	12.8	4.9		6a
2	5.7	2.7		6a
3	-12.5	5.2		
4	-25.0	5.8	Wangala Tholus	5f
5	-20.6	25.3		
6	-52.8	37.4		5k
7	-14.0	-139.2		
8	-14.9	-43.9		
9	-11.4	-43.6	Ahuna Mons	5a
10	-3.9	-36.1		5g
11	20.3	-33.7		
12	22.1	-59.8		
13	43.2	-39.5	Hosil Tholus	6h
14	4.4	-98.7		
15	-68.3	-124.0		5b
16	-19.0	-6.5		6e
17	3.9	5.1	Dalien Tholus	6a
18	56.7	-158.5		5c
19	4.1	-79.9		
20	28.4	-24.4	Aymuray Tholi	
21	41.8	9.7	Cosecha Tholus	5e
22	18.1	-50.1		
23	85.6	-0.6	Yamor Mons	
24	-43.2	-78.8	Nar Sulcus	5j
26	21.2	113.6		6b
27	-4.9	-55.1		
28	5.9	-49.2	Liberalia Mons	5i
29	38.4	-66.6	Mikeli Tholus	6g
30	32.7	-33.8	Kwanzaa Tholus	6d
32	17.2	-42.7		
33	4.4	-66.9		

*International Astronomical Union.

vapor explosion resulting from rapid heating of subsurface volatiles (Wood et al., 1978; N. Williams et al., 2014). In the second model, central pits form via the collapse of a mechanically weak icy central peak (Croft, 1983; Melosh, 1982). A third model suggests that impacts into layered “brittle/ductile” ice-rich targets produce a pit/dome morphology via uplift of the ductile lower layer and displacement of the brittle layer. Finally, a fourth model hypothesizes the formation of the central pit via collapse or draining of a “hot plug” of liquid water from the central uplift (Bray et al., 2012; Croft, 1983; Senft & Steward, 2011). Based on their analysis of Occator crater, Scully, Russell, et al. (2018) concluded that the hot plug model is most likely to have formed the Cerean central pit craters, but they emphasized that no model fully explains the observations. Testing of the proposed models in the Jupiter system has been stymied by the lack of high-resolution image data from Galileo, although abundant high-resolution data have allowed detailed analysis of Martian central pit craters (Nuhn, 2014). Recent comparative analysis of central pit craters on Mars, Ganymede, and Callisto, as well as the Moon and Mercury, suggests the possibility of new formation models while simultaneously challenging the essential role of volatiles in central pit formation (Barlow & Tornabene, 2018). Ongoing analysis of the Cerean features and comparisons to future high-resolution imaging of the Galilean satellites will likely provide insights into central pit formation as a solar-system-wide process.

3.2. Mountains and Hills

3.2.1. Large Domes

We identified two populations of positive topography features and defined two feature classes based on size and morphology: large domes and small mounds. The large domes feature class consists of 32 domical to conical mountains exhibiting relief of ~1–6 km and diameters of ~30 to 120 km (Table 3 and supporting information S1). The majority of features in this class were apparent in RC3 images, including Ahuna Mons (Ruesch et al., 2016) and the large named tholi (D. A. Williams et al., 2017). We

defined the feature class and produced the first global distribution map using RC3 and Survey images (Buczkowski et al., 2016). We expanded the feature class to include low aspect ratio features such as Liberalia Mons based on HAMO and LAMO data (e.g., Platz et al., 2018).

Figure 4 shows the global distribution of large domes, which occur preferentially in low elevation regions or planitiae. Three of these low elevation regions have been identified as potential ancient impact basins by Marchi et al. (2016). Indeed, the majority of features in the large domes class are inside or adjacent to basin B. All but two of the remaining examples are associated with basins A and C, and younger, better-preserved impact craters (e.g., Yalode and Duginavi). Ahuna Mons, which is a unique member of the feature class in terms of its extremely young age (<200 Myr; Ruesch et al., 2016), high aspect ratio, and pristine morphology, is positioned near the center of basin B and near the rim of an unnamed degraded basin that postdates basin B and predates Yalode basin to the southwest (Crown et al., 2018; Platz et al., 2018).

The majority of features in the large domes class appear to be ancient. Their surfaces are heavily cratered, and the large-scale structure of several individual features has been disrupted or modified by large impacts (e.g., Figure 5). In general, identification of geologic unit boundaries on Ceres is difficult in all but the youngest regions (e.g., Crown et al., 2018); the surface is heavily cratered at all scales and has a softened, muted character, typically with gradual transitions between terrain types. The visual homogeneity of the Cerean surface is particularly apparent in morphologic analysis of the large domes, whose surface materials are typically not distinguishable from the surrounding flat-lying terrain in terms of texture or albedo. During the LAMO-based quadrangle mapping effort (D. A. Williams et al., 2017), many of the large domes were mapped as structures inside regions of *cratered terrain*. Other, more prominent domes were mapped as *tholus material* in the quadrangle maps (e.g., Hughson et al., 2018; Platz et al., 2018); however, unit boundaries were mapped as approximate and were based on large-scale topography rather than visual differences between

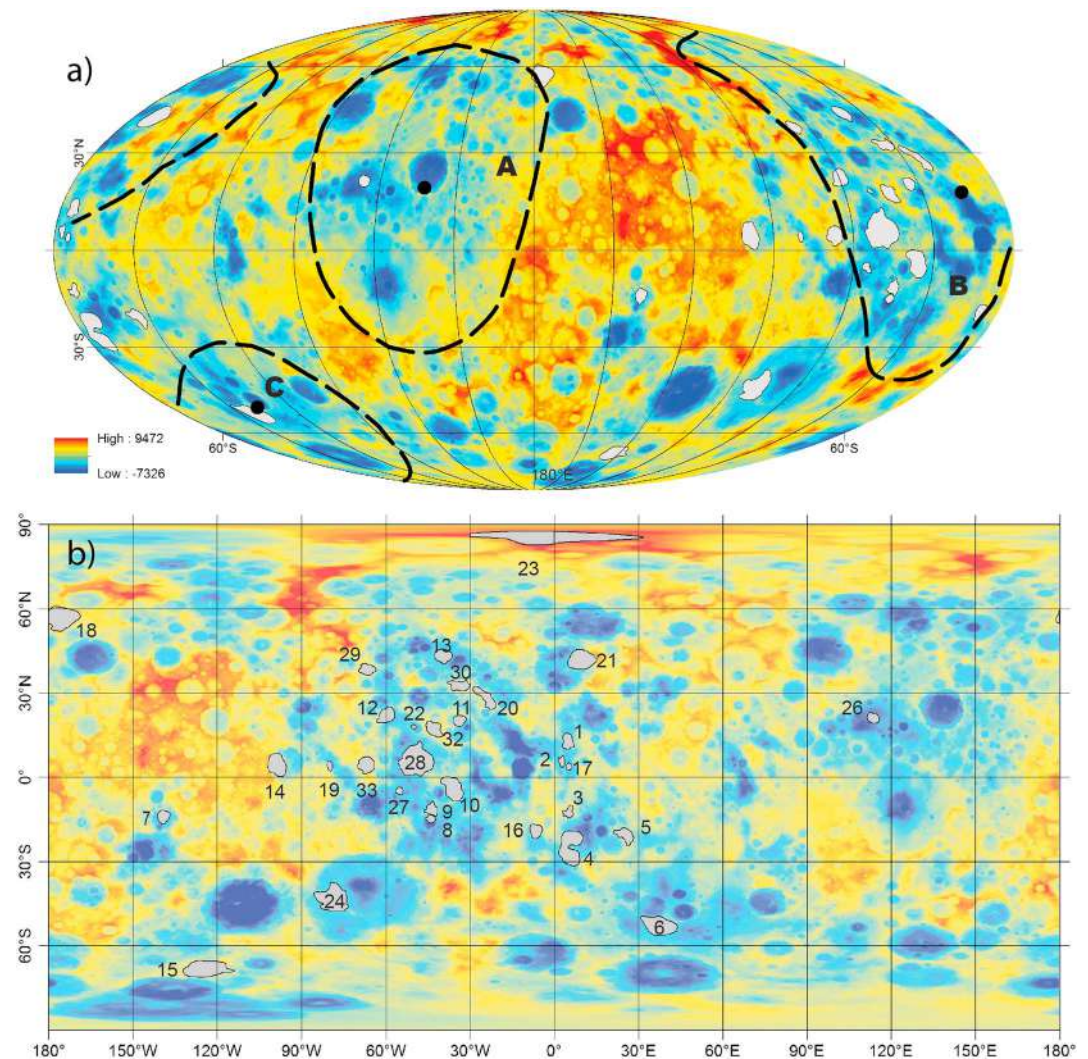


Figure 4. Global distribution of features in the *large domes* class in Mollweide (a) and equidistant (b) projections. Mountains are indicated by gray polygons; the color basemap indicates elevations derived from the High Altitude Mapping Orbit shape model (60 pixel per degree), courtesy of DLR. Domes occur preferentially in low-elevation regions and degraded impact basins (black-dashed lines) identified by Marchi et al. (2016). The majority of the identified domes are associated with basin B.

materials on and off the dome structures. The exceptional case is Ahuna Mons, which exhibits a pristine, nearly crater-free, high-albedo surface, sharp visual boundaries, and clear superposition relationships with the surrounding terrain (e.g., Platz et al., 2018; Ruesch et al., 2016).

Figure 5 shows examples of typical features in the large domes class. Figures 5a–5d highlight sharply peaked, high aspect ratio features, including Ahuna Mons, Yamor Mons, and two unnamed mountains (features 15 and 18). Three out of four features with this character occur poleward of 55° latitude. Ahuna Mons at 11° south is, again, the notable exception. Figures 5e–5h highlight more rounded, classically domical features with slightly lower aspect ratios, which are sometimes disrupted by large impact craters and occur widely in the middle and low latitudes. Figures 5i–5k show some of the most flattened features in the class, including Liberalia Mons, the large dome associated with the fracture system Nar Sulcus inside Yalode basin and an unnamed dome in the southern hemisphere.

Figure 6 shows examples of the smallest and most atypical members of the large domes feature class. A cluster of small, elongated domes to the west of Haulani crater is particularly noteworthy in this subgroup. These unnamed features exhibit relief of 1–2 km and diameters <40 km in one of the highest albedo regions on

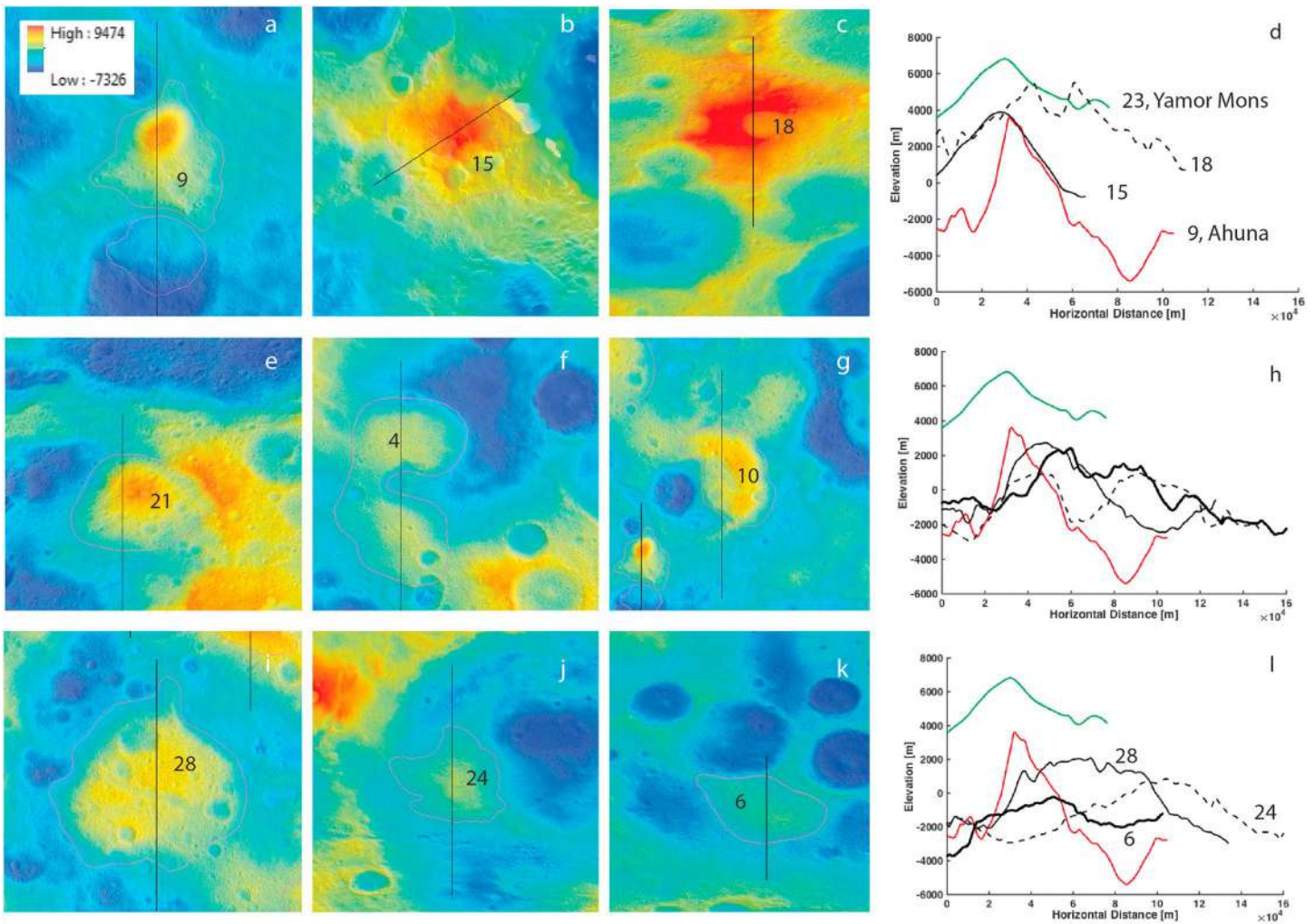


Figure 5. Examples of large domes. (a)–(c), (e)–(g), and (i)–(k) show color topography (High Altitude Mapping Orbit) overlaid on excerpts from the global grayscale image mosaic (Low Altitude Mapping Orbit), both courtesy of DLR. (d), (h), and (i) show topographic profiles across individual features highlighted in each row, respectively. In each profile panel, the profiles of Ahuna Mons (red solid line) and Yamore Mons (green solid line; not pictured) are shown for reference. (a)–(d) highlight sharply peaked mountains, including Ahuna Mons (a), Yamore Mons, and two unnamed features (b and c). (e)–(h) highlight broader, more rounded features that typify the *large domes* feature class. (i)–(l) highlight some of the broadest and most gently sloping of the domical features, including Liberalia Mons (i), and a broad fractured uplift comprising the western portion of the central ring structure in Yalode Basin (j).

Ceres. Bright ejecta material from Haulani crater blankets the domes, and their proximity to the Haulani rim suggests that the impact may have excavated material involved in dome formation. The Haulani ejecta materials show both mineralogical and morphological evidence of high volatile content, in the form of abundant carbonates and pitted materials (section 3.4), respectively (de Sanctis et al., 2016; Sizemore et al., 2017). Figure 6 also highlights a small number of diffuse features whose inclusion in the large domes feature class was marginal. Figure 6h shows a particularly ambiguous feature (#14) in the western half of Kirnis crater, which was flagged as a candidate in separate searches for domes, partially relaxed craters, and degraded landslides. We ultimately categorized it as a dome for two reasons. First, the intact western rim of Kirnis does not support a landslide interpretation. The relaxed crater interpretation is more difficult to discount; however, the northern, eastern, and southern margins of feature 14 are topographically distinct from their surroundings and round in plan form, suggesting an isolated uplift in a setting similar to Cosecha Tholus (Figure 5e, feature 21).

The broad similarities in morphology and setting of features in the large domes class suggest that subgroups of these features, or perhaps the entire class, share a common formation mechanism. Buczkowski et al.

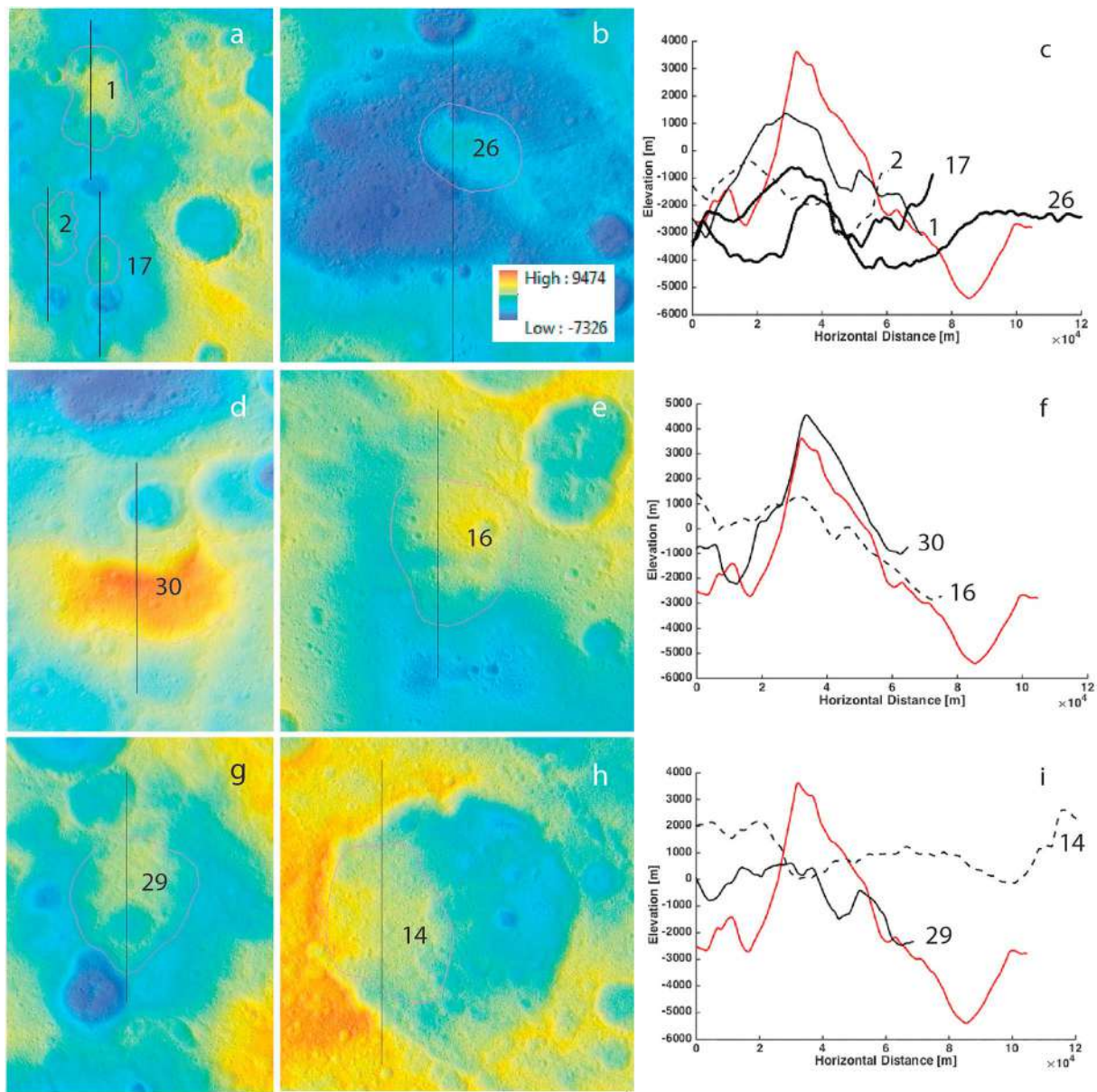


Figure 6. Examples of small, degraded, and ambiguous domical features. As in Figure 3, panels on the left show color topography (High Altitude Mapping Orbit) overlaid on excerpts from the global grayscale image mosaic (Low Altitude Mapping Orbit, 35 m per pixel), both courtesy of DLR. Panels in the right-hand column show topographic profiles across individual features highlighted in each row. In each profile panel, Ahuna Mons is shown in solid red for reference. (a)–(c) highlight some of the smaller features in the “large dome” feature class with distinct domical shapes, including three clustered features west of Haulani (a). (d)–(f) highlight two features that exhibit some ambiguity between degraded domical features and impact materials, including Kwanzaa Tholus and a small feature adjacent to a comparably sized impact crater. (g)–(i) highlight degraded features with subtle topography, including the dome in the western half of Kirnis crater.

(2016) proposed that salt diapirism or cryovolcanism might be responsible for the development of Cosecha Tholus and similar features. Based on geomorphic analysis and rheological modeling, Ruesch et al. (2016) interpreted Ahuna Mons to be a young, cryovolcanic edifice. Based on independent rheological modeling, Sori et al. (2017) speculated that lower aspect ratio features in the large domes class might represent ancient versions of Ahuna Mons, which viscously relaxed to a flatter domical shape due to moderate-to-high ice content over timescales of tens of megayears or longer. Clear morphological evidence of an extrusive cryovolcanic origin is lacking in these 31 older features. They are not associated with evidence for flow, and none exhibits summit craters that are clearly of nonimpact origin. Bland, Sizemore, et al. (2018) hypothesized that some of the domes may form via solid state ice diapirism driven by pressure

gradients in the subsurface resulting from differential topographic loading (e.g., due to crater excavation). Indeed, both intrusive and extrusive process may contribute to the observed dome population.

We have highlighted the inclusion of marginal members of the large domes class to emphasize that formation mechanisms unrelated to ice and volatiles are possible for some individual features. In particular, the history of multiple impacts everywhere on the surface introduces the possibility that individual degraded members of the large domes class were formed as central peaks or peak rings or by mutual interference of overlapping crater rims (e.g., McCoy et al., 2008). Distinguishing between features of particular geological interest and features generated by multiple impacts is a central difficulty in interpreting the morphology of Ceres or any other heavily cratered body. Despite this ambiguity for the most degraded large domes, the formation of the majority of features in the class is difficult to explain by impact processes alone.

No origin hypothesis for the unambiguous large domes has emerged that does not involve upward motion of ice, brines, or ice/brine/silicate slurries in some form. The association of the domes with large impact structures (~150–650 km in diameter) is qualitatively consistent with a cryovolcanic or cryomagmatic origin, because the impact could access deep layers of mobile material and/or produce pockets of melt (Bowling et al., 2016, 2018; Hesse & Castillo-Rogez, 2018). Fractures due to impacts could serve as conduits for mobile materials. The arrangement of dome features in the basin B region is suggestive of a relict multiring structure, suggesting fractures associated with the development of the ring structure may have been exploited by cryomagmas. Similarly, the fractured dome in western Yalode Basin (Nar Sulcus) is part of an inner ring structure; and a variety of other domes, including Ahuna Mons, occur at or near basin rims. The exposure of bright material in fresh impact craters (Haulani, Oxo) near domes (feature 21, Cosecha Tholus, and features 1, 2, and 17) is also suggestive of the involvement of volatile- and salt-rich material in dome formation. Thus, the key questions posed by the presence of these features on Ceres are the following: (1) Are individual large domes intrusive or extrusive constructs or some combination of the two? (2) What is the composition and source region of the mobile material that contributes to their formation? and (3) How old are they? Work to answer these questions is ongoing. Sori et al. (2018) compared the aspect ratios of 22 of the 32 identified domes to rheological simulations of the relaxation of Ahuna-like constructs at a range of latitudes. Their analysis indicates that the domes' observed aspect ratios are consistent with formation via extrusion of material composed of >40 vol % ice, with formation occurring over the last several 100 Myr. Bland, Sizemore, et al. (2018) have explored the alternative hypothesis that domes develop via solid state diapirism driven by buoyancy of a low-viscosity, low-density layer combined with differential topographic loading. Simulations of this process show promise for explaining the geometry of the domes located off-center in crater floors (e.g., Cosecha Tholus). Notably, these simulations require the presence of a low-viscosity, low-density material with properties similar to ice at depths of a few to >10 km. In reality, the extrusion and solid-state diapirism models are likely endmembers, and the observed large dome population may reflect a continuum of features produced by the upward movement of water-ice rich material from depth. Future analysis may be able to elucidate details of reservoir depth, cryomagma composition, and ascent mechanisms for individual features.

3.2.2. Small Mounds

Unlike the relatively homogenous large domes class, the small mounds feature class is composed of morphologically diverse features exhibiting topographic relief of hundreds of meters and diameters <10 km (Table 4 and supporting information S1). Figure 7 illustrates the diversity of the small mounds we identified; Figure 8 shows their global distribution. Based on their varied settings and morphologic diversity, individual features of the small mounds class likely do not share a single formation mechanism. They are described and cataloged here as candidate cryovolcanic or periglacial features for future investigation, although some features in this class may have been formed by impact processes that do not require a volatile rich target. We note where individual features and groups of features have greater or lesser likelihood of icy origin.

Figure 7a shows the most distinctive feature in this class, the fractured dome (~3-km diameter; ~750 m high) inside the central pit (~10 km wide; ~1 km deep) of Occator crater, with its overlying bright deposit, Cerealia Facula. Schenk et al. (2018) analyzed the morphology of this dome in the context of post impact modification of Occator crater. They proposed that it was uplifted by laccolithic intrusion or formed by volume expansion due to freezing of a reservoir of brines. Further, they argued that this uplift occurred long after the Occator forming impact. An open question in the analysis of the Occator central dome and bright deposits (faculae) is whether the liquids implicated in their formation were produced by the impact and persisted over millions of

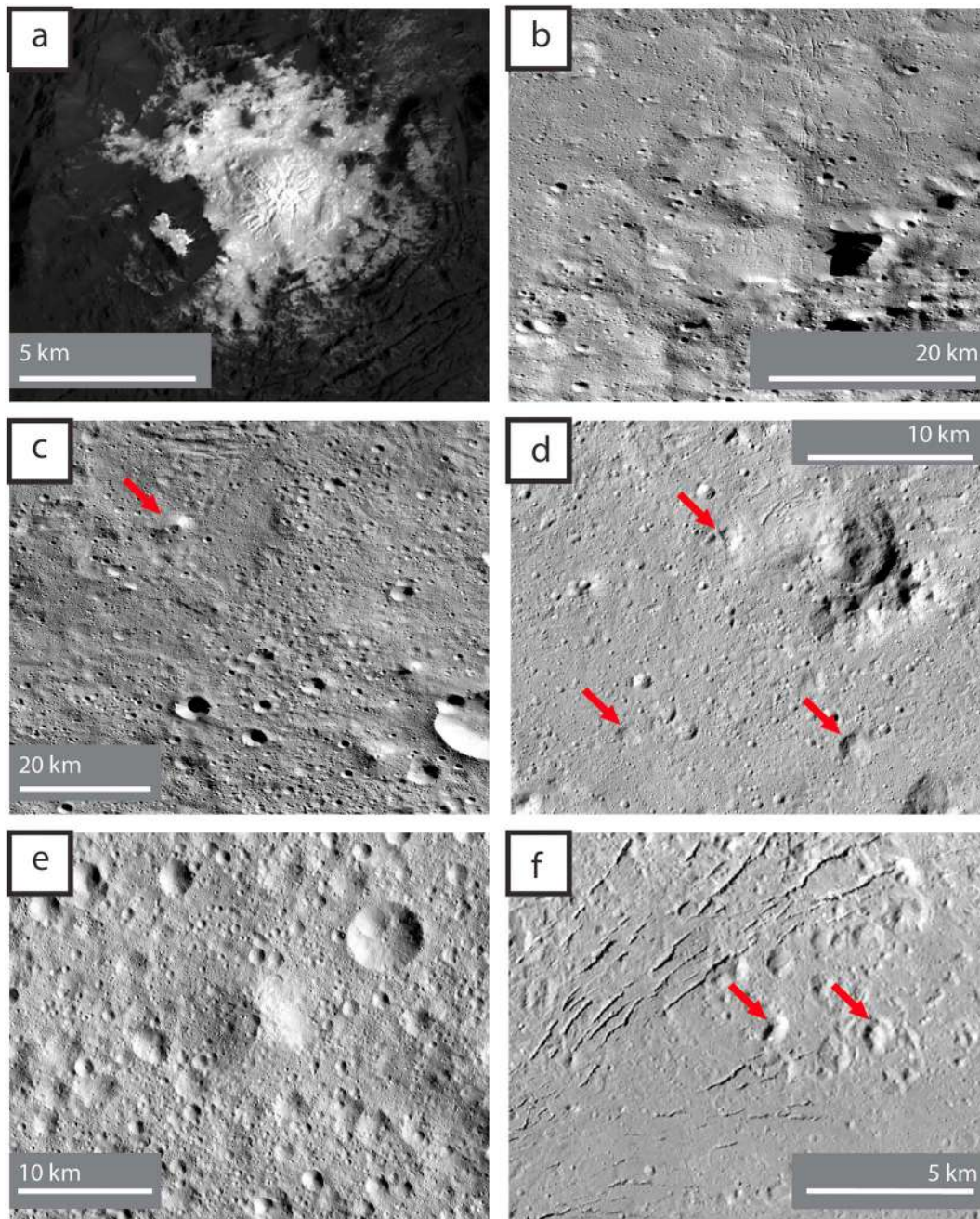


Figure 7. Examples of some of the diverse features included in the *small mounds* feature class. Red arrows indicate smaller-scale mounds. (a) Central dome at Cerealia Facula in Occator Crater, (b) south eastern floor of Urvara Crater, (c) eastern floor of Yalode Crater, (d) mounds near central pit at Gaue Crater, (e) eastern floor of Kerwan Crater, and (f) irregular mounds on southern Occator crater floor.

years (Bowling et al., 2016, 2018), or if the liquids were mobilized by the crystallization of a preexisting subsurface fluid reservoir (Quick et al., 2018), or if both mechanisms have been at play.

Figure 5b shows an irregular dome inside a surrounding moat in the southeastern floor of Urvara crater (diameter $\sim 8\text{--}9$ km). Figure 7c shows three conical hills with summit depressions on the eastern floor of Yalode crater (diameter of $\sim 2\text{--}5$ km). Notably, these features are superposed on the central ring structure of Yalode, $\sim 180^\circ$ from Nar Sulcus and its associated large dome. Figure 7d shows three small hills near the central pit of Gaue crater, one of which is disrupted by radial fractures (diameters $\sim 1\text{--}2$ km). Figure 7e shows an isolated conical hill interior to the eastern rim of Kerwan crater (diameter ~ 6 km; height ~ 1.2 km). Figure 7f shows a

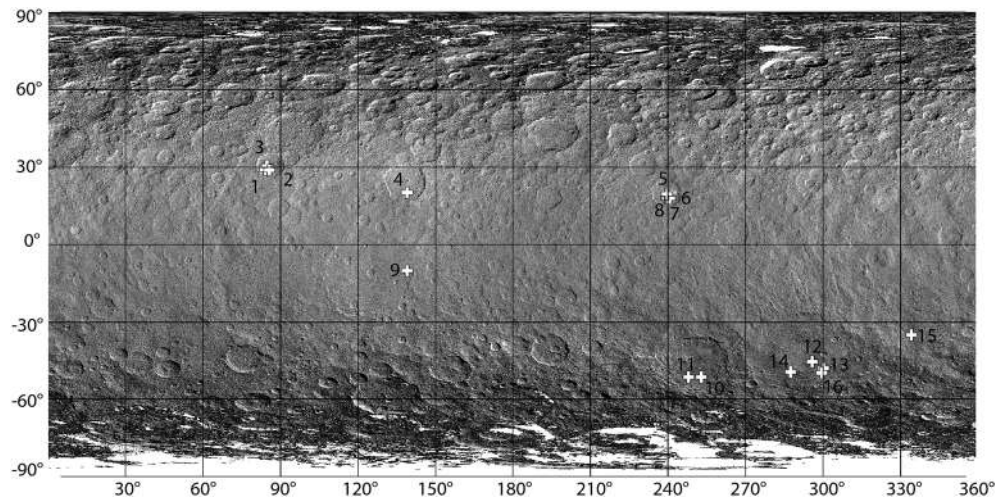


Figure 8. Global distribution of small mounds (white crosses) on the global Low Altitude Mapping Orbit mosaic (35 m per pixel) courtesy of DLR. See also Table 3.

cluster of rounded hummocks on the floor of Occator crater. Three of the Occator features (diameters $\sim 0.75\text{--}1.6$ km) are included in our catalog as explicitly marginal pingo candidates. A similar hummocky feature on the floor of Urvara (not pictured) is also included in the catalog (see below).

The Occator dome is by far the best candidate pingo or cryovolcanic feature in the small mounds class, based on its domical morphology, surface fracturing, and association with bright carbonate materials (facula). We also considered the small mounds identified in Yalode and Kerwan basins to be candidate cryovolcanoes based on their conical shape and their settings at large basin rims and central rings, which parallel the settings of many large domes. All other small domes we mapped are included in our catalog due to their occurrence in smooth crater material that has been widely interpreted as an impact melt consisting of a slurry of water, soluble salts, and boulders of silicates, insoluble salts, and perhaps ice (sections 3.4 and 3.5; e.g., Scully, Buczowski, et al., 2018). This material would be well suited for pingo development on refreezing if H_2O volume fractions exceeded $\sim 30\text{--}40\%$. The features on the floor of Gaue crater have the highest potential relevance to pingos, because one of them exhibits radial fractures analogous to fracturing observed in terrestrial and Martian permafrost settings, and similar to the Cerealia Facula dome (e.g., Dundas & McEwen, 2010). Their setting in a central pit crater also independently suggests an ice/volatile rich substrate (Hiesinger et al., 2016).

Mounds and hummocks on the Urvara and Occator crater floors are less promising pingo candidates, as their morphology is not distinct from features in the impact melt sheets of lunar craters (Hiesinger et al., 2016). Scully, Russell, et al. (2018) and Buczowski et al. (2016) interpreted them as uplifted megablocks or impact debris entrained in crater floor material. We have retained them in our catalog because hydrocode simulations of Cerean impacts and thermal arguments preclude the production of silicate melt, requiring the presence of water for ejecta fluidization (Bowling et al., 2018, 2016). Pitted materials (section 3.3) and fractures, grooves, and channels (section 3.4) associated with these two host craters also indicate the presence of water (ice or low-density phases) in the target material and resultant ejecta deposits. Future high-resolution comparisons between, for example, the Occator hummocky mounds and mounds in Gaue may yield insights into the concentration, continuity, and phase partitioning of H_2O in Ceres' ejecta deposits.

3.3. Lobate Landslides and Ejecta

We identified a variety of distinctive flow features associated with craters in early HAMO images. These features were categorized into three morphological types, based on their setting, thickness, runout length, and texture (Buczowski et al., 2016; Schmidt et al., 2017). Type 1 features (Figure 9a) typically emanate into a large crater and originate from a smaller impact structure near the large crater rim (cf. Boyce et al., 2016, and references therein). They are characterized by their vertical thickness (hundreds of meters), distinct lobate toes, surface furrows, and occurrence on steep slopes. They are interpreted as impact-triggered

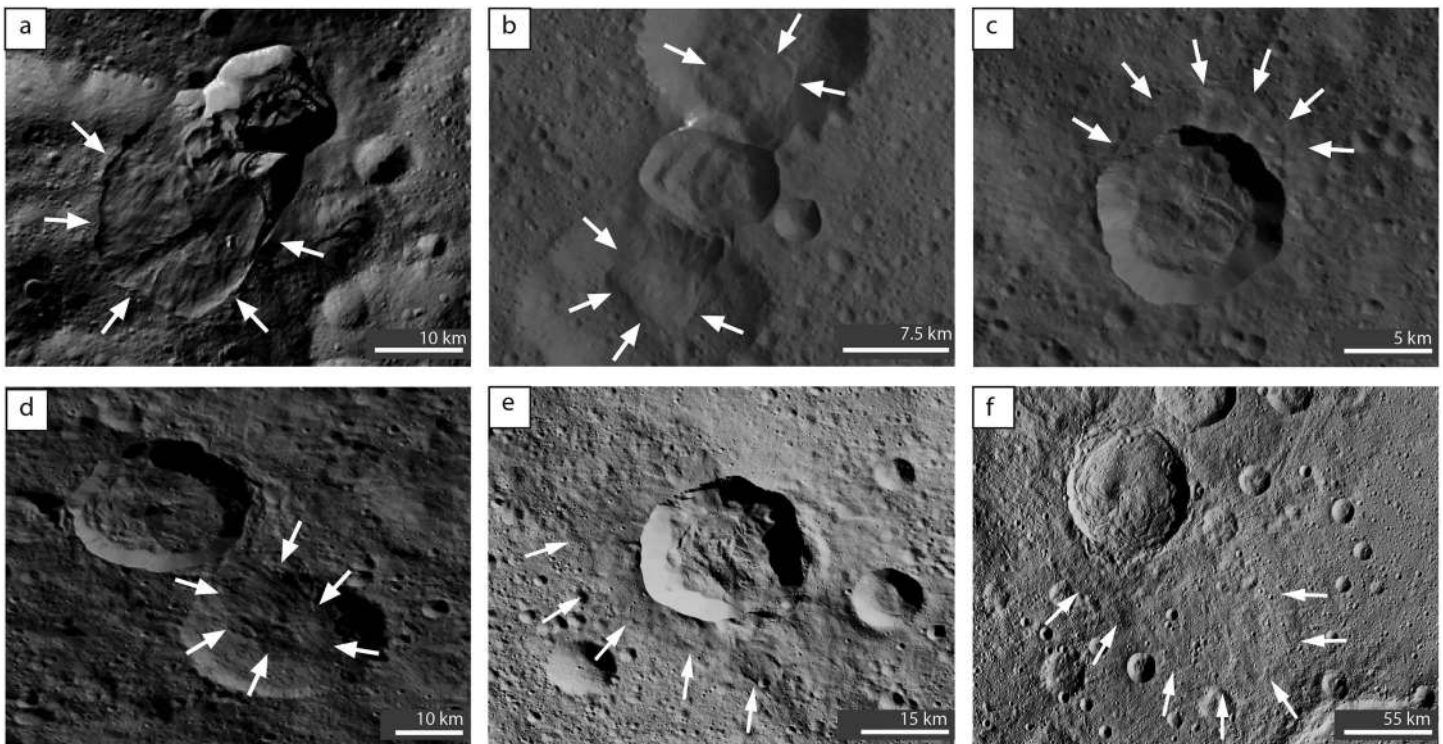


Figure 9. Examples of landslide and ejecta features discussed by Buczkowski et al. (2016), Schmidt et al. (2017), Chilton et al. (2019), Duarte et al. (2019), and Hughson et al. (2019). (a) and (b) show feature types 1 and 2, respectively, as defined by Buczkowski et al. (2016). (c) shows an intermediate type (1–2) feature as analyzed by Duarte et al. (d)–(f) show type 3 features as defined by Buczkowski et al. (2016) and the range of low (e) and high (f) mobility fluidized appearing ejecta as defined by Hughson et al. (2019).

landslides resulting from deep brittle failure and ductile creep of ice-rich material; they typically occur at latitudes poleward of 70° (Chilton et al., 2019; Schmidt et al., 2017). Type 2 features (Figure 9b) are characterized by their thinner vertical profiles, spatulate morphology, and long run-out distances on shallow slopes. They commonly originate interior or exterior to crater rims that exhibit distinctive alcoves or scars. They are interpreted as landslides with shallow failure and partial fluidization. Type 3 features (Figure 9c) are characterized by cusped, layered morphology, or “platy” texture and are interpreted as fluidized ejecta. Type 2 and 3 features preferentially occur equatorward of 60° in both hemispheres. These landslide and ejecta features are identified in both well-preserved and degraded states, suggesting that they form commonly in association with Cerean impacts and are degraded rapidly on geologic timescales (Table 4).

Mapping and analysis of lobate landslides and ejecta in LAMO data sets has broadly supported HAMO interpretations, while drawing more nuanced morphological distinctions and offering additional constraints on ice content in the depth range ~ 100 m to ~ 5 km. Identification of surface ice exposures on and near a subset of type 1 and 2 features has also strengthened the morphological case for high ice content (Combe et al., 2016, 2018). Duarte et al. (2019) described the continuum of lobate landslide morphologies observed on Ceres, highlighting landforms that exhibit combined characteristics of both the type 1 and 2 landslides, small-scale landslide features that suggest very localized enhancements in ice content, and ambiguities in the distinction between some type 2 and 3 features and their interpretation as strictly “landslides” or “ejecta.” Table 5 lists the locations and interpretations of all landslide and ejecta features in this class, including intermediate landforms.

Figure 10a shows the global distribution of landslides of all types; Figure 10b shows landslide locations relative to surface ice exposures. Chilton et al. (2019) quantified geomorphic parameters for 42 of the archetypal landslide features (13 type 1; 29 type 2), including height and runout length ratios and relationships between scar area and deposit volume. Based on these parameterizations, they estimated coefficients of internal

Table 4
Locations and Descriptions of Small Mounds

Object ID	Latitude	Longitude	Description	Figure
1	29.0	84.0	Gaue floor: dome or landslide remnant	7d
2	28.9	85.8	Gaue floor: dome or landslide remnant	7d
3	30.5	84.7	Gaue floor: fractured dome/part of peak/pit complex	7d
4	20.1	139.01	Dantu floor: oblong rise at fracture intersection	
5	19.6	−120.4	Occator: fractured dome in central pit	7a
6	17.9	−119.3	Occator: dome/knob on floor materials	
7	17.8	−120.3	Occator: knob on floor materials	7f
8	17.9	−120.7	Occator: knob on floor materials	7f
9	−10.0	138.9	Kerwan: isolated conical rise on shelf inside rim	7e
10	−51.3	−107.1	Urvara floor: dome in flooded/buried crater	7b
11	−51.4	−112.1	Urvara: knob on floor material	
12	−45.5	−64.2	Yalode: isolated conical rise, crater at summit	7c
13	−48	−59.9	Yalode: knob with summit crater, near fresh ejecta	7c
14	−49.5	−72.6	Yalode: knob, summit crater, on inner ring	7c
15	−35.1	−25.8	Isolated rise, similar to 9	
16	−49.7	−60.6	Yalode: conical rise with summit crater	

friction and made estimates of failure depth and ice content in the landslide materials. Estimated coefficients of friction for both landslide types were ~ 0.2 , consistent with the properties of cold ice ($T < 250$ K) or a variety of wet minerals. Measurements of landslide scars indicated that material failure scales with landslide size and can occur at greater depths for type 1 features (~ 1 km), while failure is always limited to a shallower depth range for type 2 features (hundreds of kilometers), suggesting differences in the cohesive strength of surface materials at high and low latitudes. Chilton et al. (2019) hypothesized that these differences arise due to latitudinal trends in ice concentration, although temperature could also play a role.

Figure 11 shows the global distribution of type 3 or fluidized appearing ejecta (FAE) features. Hughson et al. (2019) expanded the identification criteria for type 3 features beyond the smooth surface textures, broad thin appearance, and layered sets of acute cusped terminal lobes used by Schmidt et al. (2017). The new identification criteria include abruptly terminating layers, continuous and broken distal mass concentrations, superimposed layers/landslides, and channelized deposits. A notable characteristic of the ejecta features mapped in Figure 11 is that they are preferentially observed around geologically young appearing impact craters—that is, they are either a recent phenomenon or degrade quickly on the surface of Ceres. The individual features categorized as FAE often represent specific facies of larger ballistically emplaced ejecta blankets that display morphological heterogeneity but also commonly show other evidence of high volatile content and/or post depositional flow (see sections 3.4 and 3.5). Layered and fluidized ejecta are associated with craters 4.5 to >100 km in diameter. Hughson et al. (2019) modeled the emplacement of layered ejecta for all 30 identified FAE. Their results indicate that development of the lobate ejecta requires a weakly cohesive target whose material strength under impact generated strain rates is equivalent to, or less than, that of a mixture of roughly 50 vol. % water-dominated phases (ice or clathrate hydrate) and 50 vol. % strong silicate phases. Additionally, they find that the mobility of the observed FAE require a moderately low friction surface consistent with abundant ground ice starting at depths of only a few meters. The abundance of FAE craters and the variability of their mobilities suggest heterogeneities in subsurface ice content over lateral distances of a few to tens of kilometers. The depth range for which this constraint applies varies from a few to ~ 10 km, depending on crater diameter and presumed excavation depth.

Broadly, type 1 and 2 landslides are more common in the northern hemisphere than the southern hemisphere. FAE are slightly more prevalent in the south than the north but generally observed at all absolute latitudes less than 70° . Intermediate landslides are more uniformly distributed with latitude. Seasonal lighting differences could play a role in the apparent hemispheric asymmetry of the landslide distribution. The FAE occur at a broad enough range of latitudes that lighting is unlikely to have biased their identification. The modest affinity of FAE to the southern hemisphere may be linked to the slight N/S asymmetry in near-surface ice content inferred from GRaND data (Prettyman et al., 2017).

Table 5
Locations and Subtype Designations for Lobate Landslides and Ejecta

Feature subtype	Latitude	Longitude	Additional descriptors
T1	80.2	-6.5	
T1	79.4	-121.3	
T1	79.0	-3.4	
T1	78.53	38.8	
T1	76.0	-100.0	
T1	73.7	30.5	
T1	51.3	-43.9	
T1	50.8	27.3	
T1	-73.8	-108.6	
T1	-77.1	161.8	
T1	-77.4	163.8	
T1	-77.4	165.0	
T1	-77.8	166.3	
T2	79.6	39.1	
T2	65.1	-78.5	
T2	64.3	-101.2	
T2	63.7	130.3	
T2	58.6	-30.2	
T2	54.6	-104.0	
T2	53.9	126.7	
T2	52.4	129.0	
T2	51.0	26.1	
T2	50.1	-124.3	
T2	49.5	-90.6	
T2	48.9	-119.4	
T2	48.9	-90.9	
T2	46.5	-69.7	
T2	42.7	-74.2	
T2	35.5	147.6	
T2	23.4	17.5	
T2	22.3	17.5	
T2	21.8	18.7	
T2	21.4	95.1	
T2	19.7	97.6	
T2	17.3	-16.4	
T2	16.0	-155.6	
T2	12.5	-116.1	
T2	9.6	-64.2	
T2	-1.7	10.9	
T2	-3.5	10.1	
T2	-14.8	5.0	
T2	-48.7	4.4	
T2	-52.7	-24.8	
T2	-54.0	150.6	
T2	-55.4	125.0	
FAE	69.0104752	28.0836048	Channelized ejecta
T3/FAE	63.09186	-107.8788	Channelized ejecta
FAE	59.21844	-107.6419	Cuspate/lobate ejecta, possible longitudinal grooves
T3/FAE	45.3749542	-72.720505	Cuspate/lobate ejecta
FAE	42.0127106	-0.2401726	Channelized ejecta
FAE	33.7520332	45.6192055	Channelized ejecta
FAE	23.4317112	97.6586151	Cuspate/lobate ejecta
T3/FAE	19.8079586	-120.67281	Channelized ejecta

Table 5 (continued)

Feature subtype	Latitude	Longitude	Additional descriptors
T3/FAE	18.3106499	124.491585	Cusate/lobate ejecta, possible longitudinal grooves
FAE	7.742981	-154.55733	Cusate/lobate ejecta
FAE	5.7269235	10.821126	Channelized ejecta
FAE	0.6683206	-49.397076	Channelized ejecta
FAE	-6.5355973	-131.05893	Cusate/lobate ejecta
FAE	-6.705123	-141.6405	Channelized ejecta
FAE	-9.999365	21.07276	Cusate/lobate ejecta
FAE	-11.39157	-160.9316	Channelized ejecta
FAE	-19.267677	17.286047	Cusate/lobate ejecta
FAE	-32.37339	88.3822937	Channelized ejecta
FAE	-34.284657	-93.931206	Cusate/lobate ejecta
FAE	-34.762623	-81.574097	Cusate/lobate ejecta
FAE	-35.884266	168.439301	Channelized ejecta
FAE	-39.293339	110.824875	Cusate/lobate ejecta
FAE	-39.389103	173.187408	Channelized ejecta
FAE	-42.349838	-59.80312	Cusate/lobate ejecta
FAE	-47.937618	46.036087	Cusate/lobate ejecta
FAE	-54.059856	-87.681923	Cusate/lobate ejecta, possible longitudinal grooves
FAE	-54.394661	-158.40791	Cusate/lobate ejecta
FAE	-66.365273	-104.22423	Cusate/lobate ejecta
FAE	-67.293991	77.4937592	Cusate/lobate ejecta
FAE	-69.227928	2.3116858	Cusate/lobate ejecta, some longitudinal grooves
Intermediate	57.8	86.1	Contact craters
Intermediate	34.4	37.8	Rim failure
Intermediate	67.0	26.3	Small flow
Intermediate	66.7	25.5	Small flow
Intermediate	67.1	25.6	Collapsed rim
Intermediate	69.9	24.8	Talus
Intermediate	68.4	26.4	Rim failure
Intermediate	61.9	52.2	Rim failure
Intermediate	58.2	56.3	Contact craters
Intermediate	50.1	-124.3	Contact craters
Intermediate	-50.6	3.8	T2/T3
Intermediate	62.1	-105.5	Contact craters (?)
Intermediate	26.3	14.7	Rim failure
Intermediate	35.3	48.5	Rim failure, T2
Intermediate	32.4	47.6	Talus
Intermediate	-6.1	115.7	Contact craters
Intermediate	49.2	169.7	Small flow, T1
Intermediate	60.0	158.1	Contact craters
Intermediate	52.9	146.6	Contact craters
Intermediate	-57.3	-155.1	T2/T3
Intermediate	-38.3	173.1	No failure, T3
Intermediate	-40.7	168.4	T3 w T1 toe
Intermediate	-35.3	168.0	Juling crater
Intermediate	-39.7	176.9	No failure
Intermediate	59.6	-26.9	Multiple flows
Intermediate	59.2	-25.4	Contact craters (?)
Intermediate	29.4	-51.8	Contact craters
Intermediate	9.6	-64.2	Contact craters
Intermediate	36.5	-60.6	Contact craters (?)
Intermediate	6.3	-13.5	Contact craters
Intermediate	35.1	-7.2	Small flows
Intermediate	45.9	-76.1	Contact craters
Intermediate	12.7	-24.9	T2/T1
Intermediate	26.2	-25.8	Degraded rim failure
Intermediate	51.7	-44.7	Contact craters (?)
Intermediate	35.4	-55.1	Contact craters (?)

Table 5 (continued)

Feature subtype	Latitude	Longitude	Additional descriptors
Intermediate	6.6	−0.6	Protalus flow
Intermediate	26.8	−60.7	Multiple lobes
Intermediate	60.8	−111.0	Multiple lobes
Intermediate	63.3	−109.4	T2/T3
Intermediate	62.8	−109.6	Small flow
Intermediate	62.8	−109.9	T2/T3
Intermediate	18.7	−125.6	Small flow, T1
Intermediate	32.6	−135.1	Contact craters (?)
Intermediate	30.1	−138.9	Protalus flow
Intermediate	18.3	−144.4	Small flow, T1
Intermediate	48.9	−131.3	Multiple lobes
Intermediate	44.2	−74.8	No distinct toe, T2
Intermediate	1.3	−100.9	Small flow, T1/T3
Intermediate	62.0	−138.3	T2/T3
Intermediate	51.4	−79.9	Multiple lobes, small
Intermediate	30.2	−91.0	Multiple lobes, small
Intermediate	−0.1	−107.6	T2/T3 w scar
Intermediate	1.8	−108.7	T2/T3 w scar
Intermediate	64.7	−77.4	T2/T3 w scar
Intermediate	65.5	−81.7	Contact craters
Intermediate	25.7	−106.4	Small flow
Intermediate	12.5	−116.1	Plains flow, T2/T3
Intermediate	5.6	−117.0	T3
Intermediate	5.5	−119.0	Small flow, contact craters
Intermediate	4.8	−121.9	Multiple lobes, T2
Intermediate	3.5	−123.9	Protalus flow
Intermediate	7.4	−121.3	Degraded, T2
Intermediate	47.0	−120.5	T1/T2
Intermediate	34.0	−128.0	Contact craters
Intermediate	3.1	−144.9	Contact craters (?), T1/T2
Intermediate	3.2	−144.7	Protalus flow (?)
Intermediate	9.5	−160.8	Juling crater
Intermediate	31.4	−97.6	Small flow, T2/T3
Intermediate	20.8	7.9	Contact craters (?)
Intermediate	29.9	0.4	Small flow, contact craters
Intermediate	−47.7	19.1	Small flow
Intermediate	−38.6	48.5	Small flow
Intermediate	14.3	79.9	T1/T2
Intermediate	20.7	101.4	Contact craters
Intermediate	6.7	88.9	Degraded, T2
Intermediate	−70.2	2.9	Multiple flows (?), T2
Intermediate	−35.5	167.6	Contact craters (?), T2/T3
Intermediate	26.8	131.1	Protalus flow
Intermediate	−3.4	144.2	Contact craters
Intermediate	−24.6	137.0	Failed ridge wall
Intermediate	22.3	160.5	Failed ridge wall
Intermediate	20.2	159.7	Failed ridge wall
Intermediate	20.0	159.7	Failed ridge wall
Intermediate	6.9	150.0	Failed ridge wall
Intermediate	−23.3	57.2	Failed ridge wall
Intermediate	−42.8	45.8	Small flow
Intermediate	33.8	95.7	T2/T3
Intermediate	37.9	86.3	T2/T3
Intermediate	24.2	19.1	T2/T3
Intermediate	−30.3	−156.2	Contact craters (?)
Intermediate	−38.5	−93.6	Multiple flows (?)
Intermediate	−39.0	−94.1	T2/T3
Intermediate	−40.0	−94.9	Multiple lobes
Intermediate	−40.3	−95.3	Contact craters
Intermediate	−40.9	−95.8	T2/T1
Intermediate	−41.1	−96.3	Contact craters

Table 5 (continued)

Feature subtype	Latitude	Longitude	Additional descriptors
Intermediate	31.4	−69.9	T2/T1
Intermediate	−37.3	177.2	Multiple lobes, T1/T2
Intermediate	−38.6	178.2	T2/T3
Intermediate	−37.6	178.7	Rim failure, T1/protalus
Intermediate	21.7	−168.0	T2/T3
Intermediate	−44.6	153.3	Multiple lobes, T1
Intermediate	−40.9	112.0	Contact craters
Intermediate	54.9	73.6	T2/T3
Intermediate	−77.4	165.0	Small flow
Intermediate	−43.0	38.0	Small flow
Intermediate	−34.0	90.9	Contact craters (?)
Intermediate	54.4	95.1	Protalus flow
Intermediate	68.0	−97.2	Rim failure, T1/T2
Intermediate	−53.6	−84.3	Rim failure, multiple lobes
Intermediate	−54.9	−84.6	Contact craters
Intermediate	−7.6	−139.5	Contact craters
Intermediate	−33.7	−95.6	Degraded, T2/T3
Intermediate	58.5	−96.8	Contact craters (?)

Note. See Chilton et al. (2019), Hughson et al. (2019), and Duarte et al. (2019) for discussion of high mobility and low mobility ejecta and intermediate landslide subtypes. FAE = fluidized appearing ejecta; T1, T2, T3 = type 1, type 2, type 3.

3.4. Pits, Depressions, and Scarps

Our search for morphology linked to sublimation focused on identification of pits, depressions, and scarps and took advantage of the progressive improvement in spatial resolution that occurred over the course of the primary mission at Ceres. As early as RC3, it was apparent that Ceres' surface morphology is dominated by impact structures. Thus, distinguishing between features produced by gas-phase volatile loss and features produced by primary and secondary impacts was an ongoing consideration in our search.

Notably, our searches of RC3, Survey, and HAMO data showed no evidence of pits or depressions meeting our search criteria (section 2.1.3). This null result was consistent with predictions that surface ice deposits would be localized, rare, and transient on Ceres. It also suggested a lack of extended shallow (upper 1–100 m) subsurface deposits of highly concentrated “clean” ice and/or slower rates of ice loss than had been predicted prior to Dawn's arrival at Ceres. This result was consistent with other, contemporaneous evidence that ice comprised <30–40 vol. % of the upper meters to kilometers of Ceres subsurface (Bland et al., 2016; Prettyman et al., 2017).

We ultimately observed pitting in LAMO images (35 m per pixel), which revealed localized clusters of round-to-irregular, apparently rimless pits incised in smooth impact materials associated with seven young complex craters (Table 6 and supporting information S1; Sizemore et al., 2017). These pitted regions are mapped in the feature class pitted materials (Figure 12). Their settings and morphology exhibit striking similarities to pitted materials previously discovered by Dawn at Vesta (where the presence of ice is debated; Denevi et al., 2012; Scully et al., 2015), and pitted materials identified in low latitude and midlatitude Martian craters (where ice is implicated in pit development; Boyce et al., 2012; Tornabene et al., 2012). Sizemore et al. (2017) interpreted the Cerean pitted materials to result from rapid outgassing of H₂O and OH from a thin layer (tens to hundreds of meters) of hot (>300 K) brecciated material. This interpretation hinged on two arguments. First, the Cerean pits are morphologically distinct from pits and depressions thought to result from long-term sublimation elsewhere in the solar system. The Cerean pits typically exhibit round-to-irregular margins and sloping walls, rather than elongated branching shapes and flat floors, and pit size is correlated with host crater diameter. Second, recently modeled H₂O sublimation rates for Ceres (meters per gigayear; Landis et al., 2017; Schorghofer, 2016; Sizemore et al., 2017) are too slow to produce the observed pit relief (>100 m) during the short time since the formation of the host craters (typically <100 Myr). Sizemore et al. (2017) concluded that although impact heating was necessary for pit formation on Ceres, H₂O sourced from ground ice was the dominant volatile lost in the process. This conclusion was based on thermal arguments and extensive observational evidence for modest quantities (20 to <40 vol %)

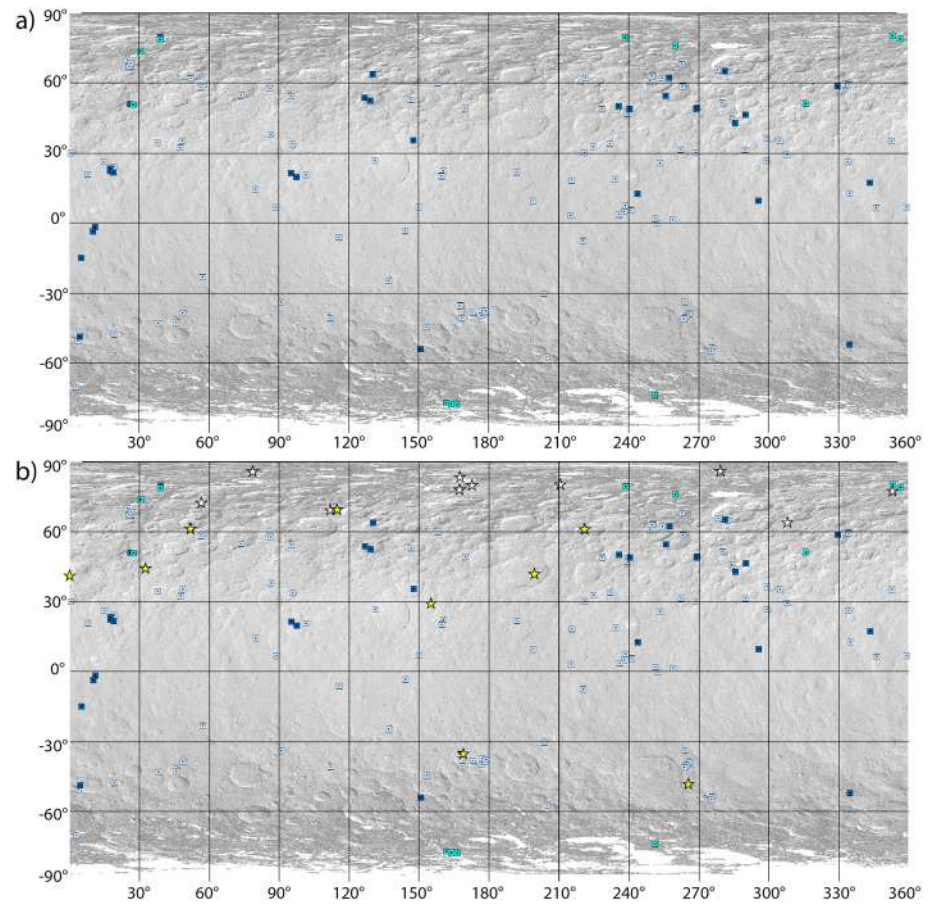


Figure 10. Global distribution of lobate landslides. (a) Type 1 landslides are cyan squares; type 2 are dark blue squares; intermediate type landslides are light blue squares. (b) Landslide features are denoted as top panel; permanently shadowed region bright spots (Platz et al., 2016) are shown as white stars; Visible and InfraRed Mapping Spectrometer surface ice detections are shown as yellow stars (Combe et al., 2018). The base image in both panels is the global Low Altitude Mapping Orbit mosaic (35 m per pixel) courtesy of DLR.

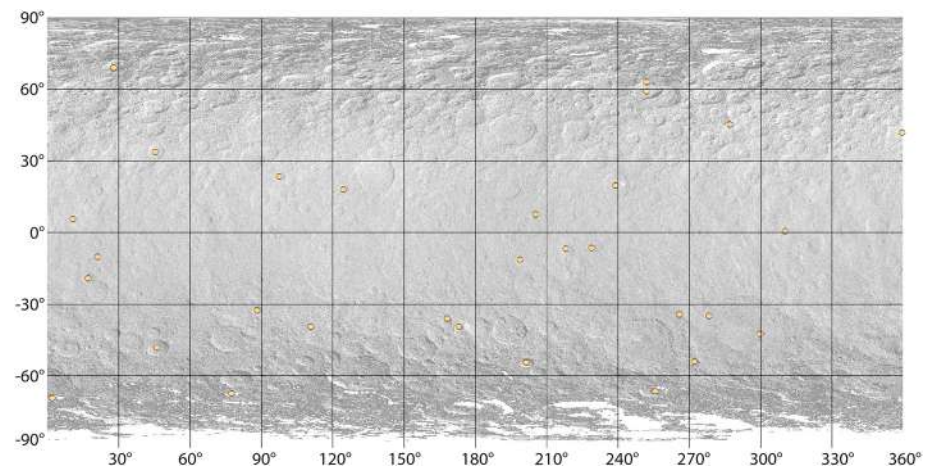


Figure 11. Global distribution of fluidized appearing ejecta. Crater centers are indicated by tan circles. The base image is the global Low Altitude Mapping Orbit mosaic (35 m per pixel) courtesy of DLR.

Table 6
Summary of Midlatitude Craters Hosting Pitted Materials and Fractures, Grooves, and Channels

Crater	Diameter	Latitude	Longitude	Pitted materials	Circumferential fractures	Large floor fractures or faults	FFC designation	Channels	Central feature
Yalode	260	−42.58	292.48		Yes	Yes		Yes	Ring/depression
Urvara	170	−45.66	249.24	Degraded	Yes	Yes		Yes	Peak/ridge
Dantu	126	24.30	138.23	Yes	Yes	Yes	Class 1	Yes	Ring
Ezinu	116	43.24	195.70		No	Yes	Class 1		None
Occator	92	19.82	239.33	Possible, degraded	Yes	Yes	Class 1	Yes	Pit (with interior dome)
Gaue	80	30.81	86.16		No	Yes	Class 1		Pit/ring
Kaikara	72	42.82	222.43		No	No			Pit/ring
Jarimba	69	−24.08	21.25		Yes	No			Peak and/or pit, degraded
Rongo	68	3.21	348.71		Possible	No	Class 4		Peak, hummocky
Fejokoo	68	29.15	312.11		No	No			Peak, hummocky
Consus	64	−20.7	200.5		Yes	No			Hummocky, ring?
Ikapati	50	33.84	45.61	Yes	Yes	Yes	Class 1		Peak
Azacca	50	−6.66	218.40	Possible, degraded	Yes	Yes	Class 1		Peak/ridge
Kondos	44	−19.34	17.31		Yes	No	Class 4		Peak, hummocky
Messor	40	49.93	233.73		No	No	Class 4		Peak/ridge, hummocky
Ninsar	40	30.3	263.26		No	No	Class 4		Peak, hummocky
Lociyo	37.8	−6.53	228.83		Yes	No	Class 4		Peak, hummocky
Tupo	36	−32.35	88.38		Yes	No	Class 4		Peak, hummocky
Aristaeus	36	23.43	97.68		Yes	No			Peak, hummocky
Haulani	34	5.80	10.77	Yes	Yes	Yes	Class 1		Peak/ridge
Kokopelli	34	18.30	124.50		No	No	Class 4		Peak, hummocky
Nepen	26.4	6.19	220.54		No	No	Class 4		Peak, hummocky
Kupallo	26	−39.44	173.20	Yes	Yes	Yes	Class 1	Yes	Peak/ridge
Cozobi	24	45.33	287.31		Yes	No			None/hummocky
Unnamed	20.8	50.04	238.5		No	No	Class 4		Peak, hummocky
Juling	20	−35.90	168.48		Yes	Yes	Class 4		None/hummocky
Unnamed	18.9	−8.5	315.37		No	No	Class 4		None/hummocky
Unnamed	15	−23.00	279.00		Possible	No	Class 4		None
Unnamed	13.6	43.52	202.48		No	No	Class 4		None/hummocky
Unnamed	10.8	−8.34	312.6		No	No	Class 4		None/hummocky

Note. Craters with a class 4 FFC designation are also noted. FFC = Floor Fractured Crater.

of surface and subsurface ice on Ceres (Bland et al., 2016; Combe et al., 2016; Prettyman et al., 2017; Schmidt et al., 2017). However, abundant clathrates and hydrated salts could reduce the dominance of conventional water ice (Bland et al., 2016; Fu et al., 2017).

In addition to the pitted materials analyzed by Sizemore et al. (2017), we identified a small number of isolated irregular depressions and scarps and defined a feature class of the same name (Figure 13). The depressions and scarps feature class includes two elongate, flat-floored depressions in the smooth materials interior to Azacca and Occator craters, an elongated branching depression with rounded margins on the Yalode floor, and a small complex of angular scarps on the Occator ejecta. Like the pitted materials, these features occur in smooth ejecta deposits associated with young complex craters. The morphology of the two flat-floored depressions in Azacca and Occator is clearly distinct from the clustered pits and potentially more consistent with long-term sublimation than with rapid high-temperature outgassing. However, the same dynamical arguments that constrain the process of pit development apply to the flat-floored depressions; enhanced temperature and/or locally enhanced ice concentration are required to invoke gas phase ice loss as the mechanism that produced the observed topography over the age of the host crater. Alternatively, the flat-floored depressions could have developed due to post depositional flow of the smooth ejecta material in which they occur. Both scenarios indicate rapid postimpact feature development and some availability of water or ice. The unique depressions and scarps on the Occator ejecta (Figure 13c) and the elongate branching depression on the Yalode floor may reflect modification of fractures (section 3.5) in

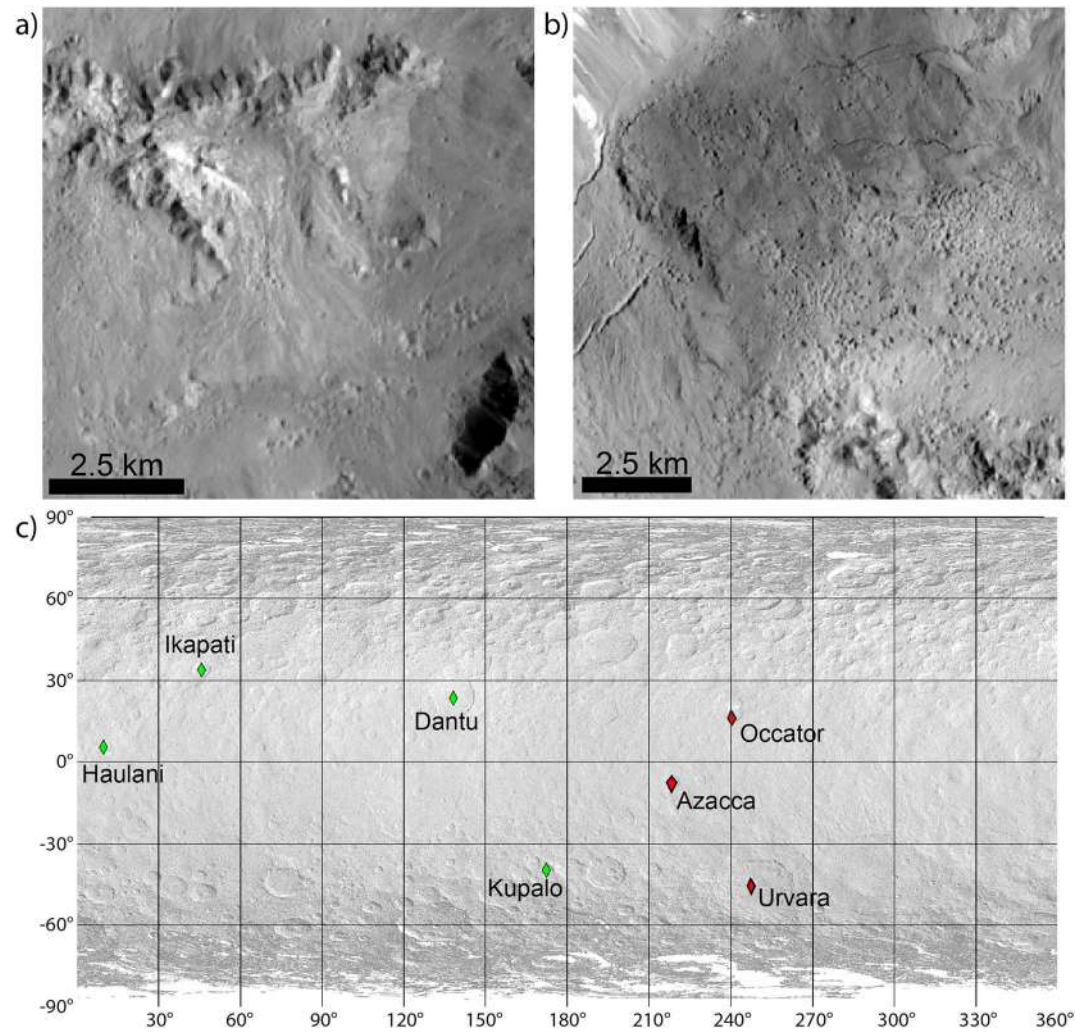


Figure 12. Ceres' pitted materials. Examples of pits (a) on smooth material with evidence of flow (surface lineations, embayment relationships, and lobate margins) and (b) near fractures, both on the floor of Haulani crater. (c) Global distribution of craters hosting pitted materials. Green diamonds indicate well-preserved *pitted materials*; red diamonds indicate degraded examples. The base image in (c) is the global Low Altitude Mapping Orbit mosaic (35 m per pixel) courtesy of DLR.

smooth ejecta, perhaps via sublimation of volumetrically abundant ice. We emphasize that these unique features may have been created by processes unrelated to ice or volatiles (e.g., Bray et al., 2010); their morphology and setting are merely suggestive.

From a global perspective, morphological evidence for gas-phase ice loss on Ceres is localized, and the quantitative inferences about subsurface ice content that can be drawn from these features are limited. The pitted materials are confined to 5–7 young (<700 Myr) impact craters in the mid- and low latitudes. The observation of progressively more degraded pits in the “older” host craters suggests that pits are destroyed rapidly on geologic timescales, and they may form commonly in Cerean impacts. Based on impact temperatures predicted by hydrocode simulations (Marchi et al., 2013) and comparisons between Martian and Cerean pitted materials, pitted materials were likely produced at locations where peak temperatures exceeded 300 K (Sizemore et al., 2017) and H₂O-dominated phases (ice and clathrates) comprised <50 vol. % of the brecciated/fluidized layer in which the pits formed. Thus, the occurrence of pitted materials throughout the low latitude and midlatitudes is consistent with other evidence that conventional ice and/or H₂O bearing phases have been excavated from depths of a few to >10 km and that some of this water is retained as ice in shallow (tens to hundreds of meters thick) ejecta deposits today. This result applies

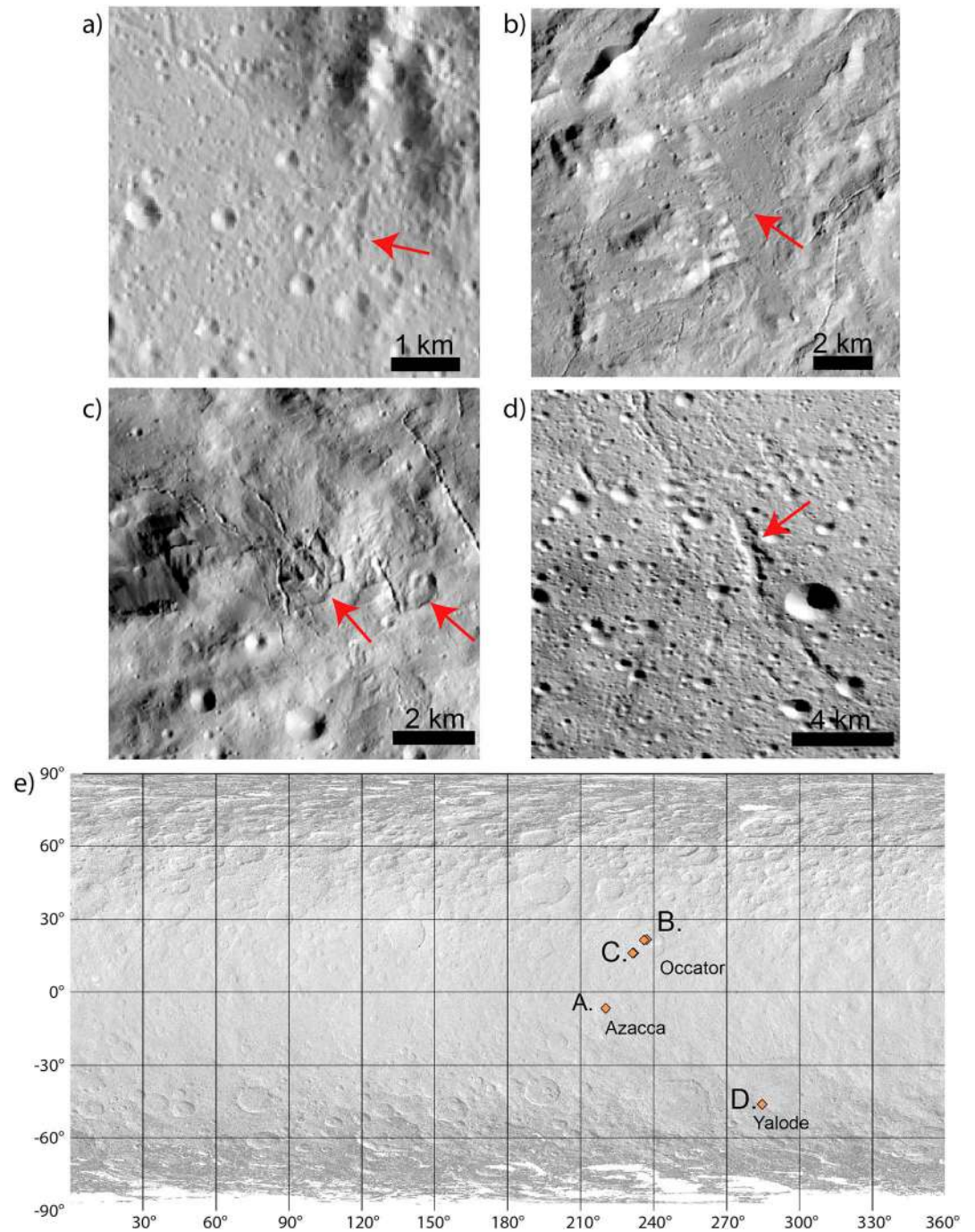


Figure 13. Features in the *depressions and scarps* feature class, which include (1) flat-floored depressions on the floors of Azacca (a) and Occator (b) craters, (2) angular scarp-bounded depressions on the Occator ejecta blanket (c), and an elongate rounded depression on the Yalode floor (d). Unlike the *pitted materials* feature class, the identified depressions and scarps are diverse and are not linked to a common development process. (e) shows their global distribution; base image is the global Low Altitude Mapping Orbit mosaic (35 m per pixel) courtesy of DLR.

specifically to middle and low latitude regions where ice is buried too deeply (>1 m) for detection by GRaND. The absence of pitted materials and their characteristically flat-floored host craters at high latitudes also suggests that a temperature threshold must be reached for these features and their host ejecta facies to develop.

3.5. Fractures, Grooves, and Channels

In direct analogy to Mars, Ceres' pitted materials occur in smooth, ponded ejecta material, proximal to extensive evidence of post depositional flow of the ejecta (including curvilinear to sinuous streamlines, embayment of high standing topography, teardrop shaped "islands," and lobate margins). Also, in direct analogy to Mars, Ceres' pitted materials are commonly associated with linear grooves and fractures in the host crater floor (Sizemore et al., 2017; Tornabene et al., 2012). In the Cerean craters that contain pitted material, grooves and fractures also occur on smooth ejecta external to the crater rim and on interior terraces.

Based on the common association of fractures and grooves with pitted materials and other indicators of high volatile content, we carried out a global mapping of small-scale linear features (lengths of 500 m to tens of kilometers; widths <3 km). The resultant feature class, fractures, grooves, and channels, includes four distinctive subgroups of features that commonly occur together and grade into one another at some locations; "floor fractures," "circumferential fractures," "troughs," and "channels." Figure 14 shows a global mapping of all fractures, grooves, and channels, along with examples of the subtypes. Figures 12b and 12c show the large-scale pattern of fractures at Occator and Ikapati craters, respectively. In both cases, the crater floors host linear features (tens of kilometers long, hundreds of meters up to >2 km wide, and tens to ~100 m deep, with a characteristic v-shaped depth profile) that grade into smaller grooves and pit chains that align with and crosscut the larger features. We refer to these large features as floor fractures and their host craters as "Floor Fractured Craters" or "FFCs," based on a proposed analogy with similar features observed in lunar and Martian craters (Schultz, 1976; Buczkowski et al., 2018). We refer to the smaller adjacent features (<200 m wide; tens of meters deep or less) generically as grooves or fractures. Figures 12b and 12c also show populations of circumferential fractures on the terraces, rims, and ejecta blankets of the two craters. Circumferential fractures are typically, but not always, smaller than floor fractures (<500 m wide; tens of meters deep or less). Like the small-scale fractures on the crater floors, they typically appear as grooves or pit chains incised in the surrounding smooth material and are distinguished from generic grooves or fractures only by their setting and orientation with respect to the host crater.

Figure 14d shows the largest linear features included in our mapping, the system of troughs and ridges designated as Nar Sulcus, which is collocated with a large dome inside Yalode basin. Individual troughs comprising Nar Sulcus are >50 km long and exhibit topographic maximum topographic relief >300 m. At its western end, Nar Sulcus grades into smaller-scale, straight grooves or fractures (typically <300 m wide; ~100 m to kilometer long; tens of meters deep or less). Figure 14d also shows a population of small-scale grooves and channels oriented down slope from and nearly perpendicular to Nar Sulcus. Features designated as channels are visually similar to generic grooves and fractures but are distinguished by their tendency to be narrower, shallower, and to be curvilinear to sinuous. Channels sometimes exhibit junctions, forming immature or proto-networks that follow the local slope direction (Crown et al., 2018). Figure 14e shows another example of channels in the Urvara basin, likewise associated with a prominent trough/ridge system in the basin floor. Other examples of channels occur at Occator and Ikapati craters, where small-scale linear features grade into areas of apparent bulk flow of smooth ejecta (Crown et al., 2018).

In the global view (Figure 14a), fractures, grooves, and channels serve as markers of the smooth, apparently fluidized materials associated with the youngest complex craters and a small number of simple craters on Ceres. They are confined to mid- and low latitudes, suggesting again that a temperature threshold must be met for the production of the smooth material in which they occur. Several lines of reasoning indicate that fractures, grooves, and channels develop because both the impact target material and the resultant ejecta are water rich. In their initial global assessment of Ceres' geomorphology, Buczkowski et al. (2016) identified eight large craters with prominent floor fractures and 13 smaller craters with hummocky floors and interior moats suggestive of floor uplift but lacking floor fractures. They designated these craters as class 1 and class 4 FFCs respectively, based on morphological analogies with the Moon. Buczkowski et al. (2018) later extended this analogy to hypothesize that the Cerean FFCs form via cryomagmatic intrusion or diapirism beneath the crater floor. They specifically argued that the presence of interior moats in the class 4 FFCs precluded crater relaxation and required subsurface inflation (Dombard & Gillis, 2001). Buczkowski et al. (2018) did not include Urvara and Yalode craters in their list of designated class 1 FFCs, because the large systems of parallel fractures associated with localized uplift in the Urvara and Yalode floors (termed troughs in our discussion for clarity) are morphologically distinct from the floor fractures in, for example, Occator and Dantu. In

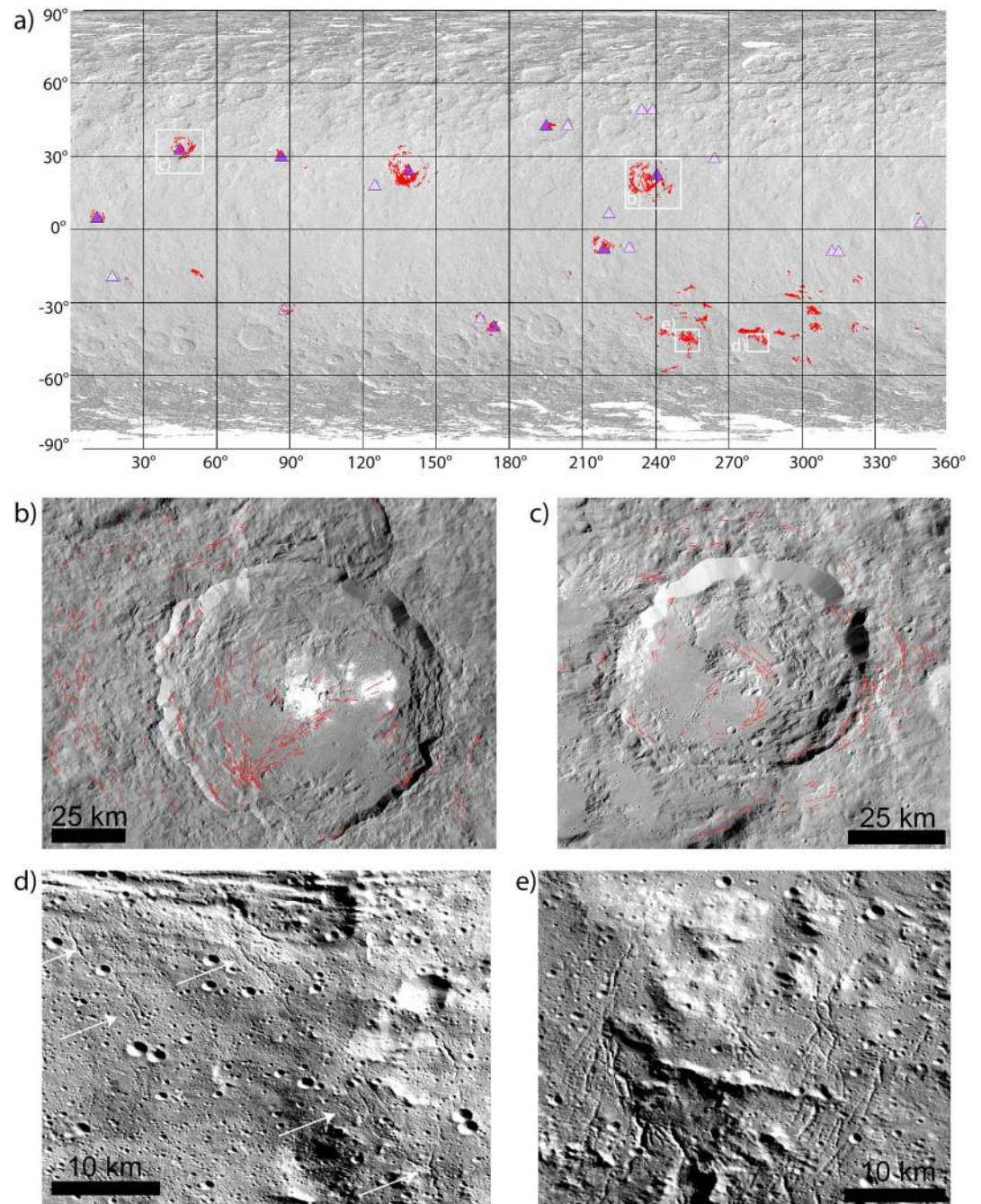


Figure 14. (a) Global map of all *fractures, grooves, and channels* (red lines); dark purple triangles indicate designated class 1; light purple triangles indicate and class 4 Floor Fractured Craters; (b) floor fractures and circumferential fractures at Occator Crater; (c) floor fractures and circumferential fractures at Ikapati Crater; (d) example of toughs (top of panel running left to right) and channels (middle of panel) in Yalode crater, (e) example of channels in Urvara crater.

our mapping, we treated the troughs as part of a continuum of fracture, groove, and channel subtypes that grade into one another, are sometimes difficult to distinguish visually without regional context, and may arise via common processes. Our analysis indicates that Urvara and Yalode, all the identified class 1 FFCs, and roughly half of identified class 4 FFCs also exhibit circumferential fractures.

Otto et al. (2019) conducted a detailed mapping of circumferential fractures at three craters (Azacca, Ikapati, and Occator) and used numerical models of postimpact relaxation to compare model stress fields to observed

fracture geometry at Azacca. They concluded that circumferential fractures likely result from the relaxation of a crater in a layered subsurface. Model scenarios that produced the observed fracturing included a layer of low-viscosity material (10^{20} Pa s) 2–9 km thick, underneath 1 km of rigid overburden (10^{25} Pa s). The ductile behavior of the lower layer is best explained by a relatively high abundance of buried ice (Otto et al., 2019), although impact heating may play a role. The viscosity requirements imposed by Otto et al. (2019) are not unique to ice, but simulations of Ceres' thermal evolution suggest that salts are not available in sufficient abundance to drive the mechanical behavior of the crust, although they could be locally concentrated in lenses (see section 4.3). Although Otto et al. (2019) invoked relaxation of the low viscosity layer to explain the development of circumferential fractures, they observed that craters exhibiting these fractures were *not* shallower than Ceres' average as a group. This observation is consistent with the assertion by Buczkowski et al. (2018) that a mechanism other than relaxation is required to explain the low d/D of FFCs as a group. However, it also points to a need for further self-consistent analysis and modeling of these overlapping crater populations. Until that analysis is more mature, FFC is best used as a descriptive term at Ceres.

The apparent fluidization of the ejecta facies in which small-scale fractures, grooves, and channels are incised is itself suggestive of volatile involvement and initially motivated the inclusion of these features in our catalog. Crown et al. (2018) speculated that channels in the Urvara and Yalode floors developed via a sequential process of fracture, collapse, and localized sapping and flow. This interpretation implies at least localized saturation of the ejecta material by fluids, which are likely preserved as ice today. Similarly, the irregular depression on the Occator ejecta (Figure 13c) and the elongate branching depression in the Yalode floor (Figure 13d) described in section 3.4 are closely associated with fracture and channels; they may represent instances of modification of small fractures via sublimation of pore saturating or volumetrically excess ice.

3.6. Features Not Identified

Systematic searches for polygonal patterned ground and Martian-style “basketball terrains” did not yield any identifications. This null result does not strictly rule out the occurrence of thermal contraction polygons on Ceres. Polygons smaller than ~200 m would not be resolved in LAMO images (~35 m per pixel), and as anticipated, lighting conditions presented a challenge to high-latitude feature searches. However, two lines of evidence suggest thermal contraction polygons may *not* develop commonly on Ceres. First, analysis of GRaND data indicates ice volume fractions in the upper meter of the high latitude regolith are ~20 vol. % (Prettyman et al., 2017), significantly less than the pore volume of most soils and regolith simulants, which commonly fall in the range ~30% to 65% (Sizemore & Mellon, 2008). Undersaturation of the pore space by ice implies that the tensile strength of Ceres' upper 1–5 m is low compared to the ice-saturated and/or ice-dominated materials common on Mars. Sufficient stress may never develop for fracturing to occur due to thermal contraction. Second, our search for morphological evidence of sublimation yielded a limited set of identified features (section 3.4) and indicated that impact craters dominate surface textures down to the limit of resolution on all but the youngest terrains. On Mars, polygon development rapidly erases small craters. The opposite may be true on Ceres.

3.7. Features Not Mapped

In the currently available data sets, four types of distinctive morphological features are commonly associated with Ceres' young, complex, midlatitude craters. These include lobate and layered ejecta facies (lobate landslides and ejecta, type 3), pitted materials, scarps and depressions, and fractures, grooves, and channels described in sections 3.3, 3.4, and 3.5. In addition, a variety of gully-like mass-wasting features occurs in midlatitude crater walls near pitted materials. These mass-wasting features may have relevance to ice and water by analogy with Mars, where floor fractures and gullies are also commonly associated with pitted materials (Boyce et al., 2012; Tornabene et al., 2012). Specific gully morphologies associated with pitted terrains on Vesta have been attributed to debris-flow motion of materials mobilized by relatively small amounts of liquid water sourced from ice in the Vestan target material (Scully et al., 2015). Similar arguments may apply to the Cerean features, but candidate gullies are not mapped or discussed here. Evidence for ice and transient liquid water on Vesta is debated (Denevi et al., 2012), and nearly 20 years of research dedicated to classifying Martian gully morphology and understanding the role of water in gully formation has been inconclusive (e.g., Dickson et al., 2007; Diniega et al., 2013; Dundas et al., 2010; Malin & Edgett, 2000; Mellon &

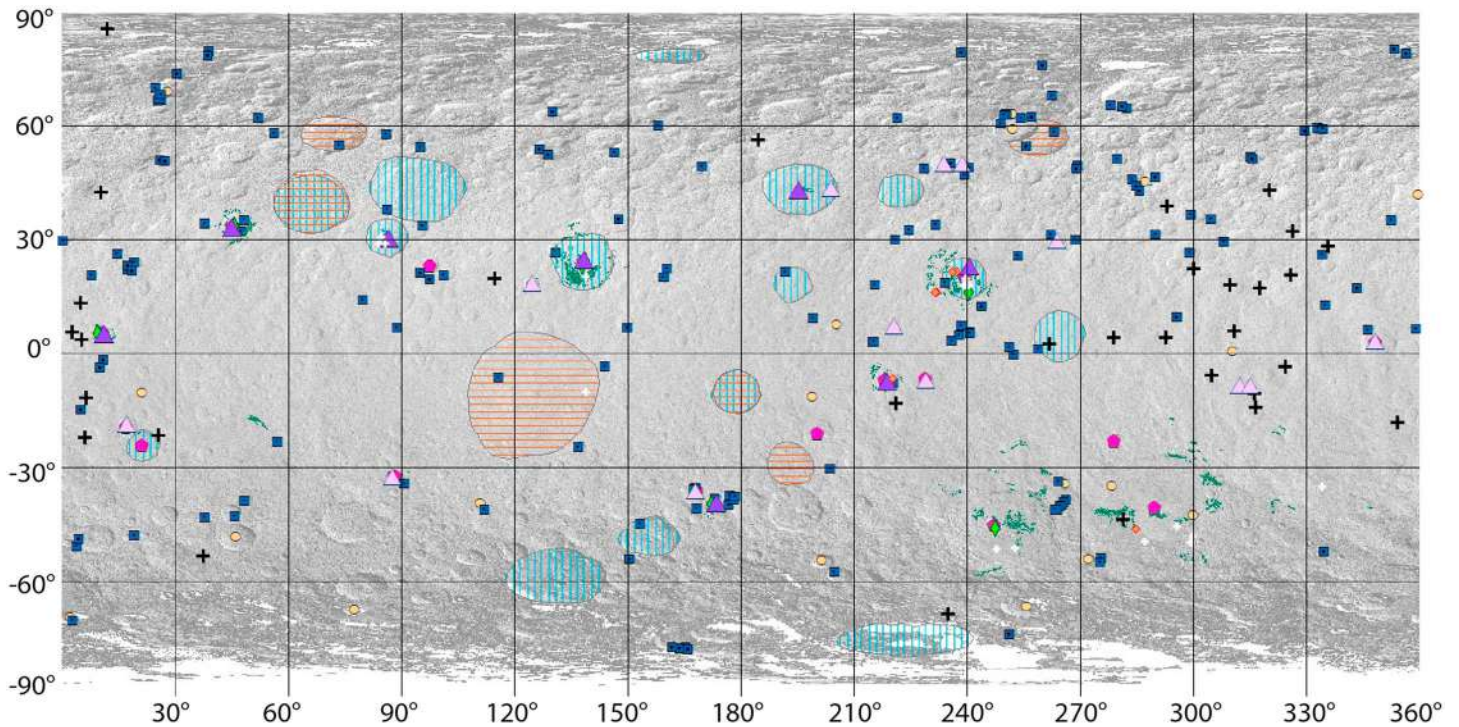


Figure 15. Global view of all cataloged features. Polygons with horizontal orange hash marks indicate relaxed craters. Polygons with vertical blue hash marks indicate central pit craters. Light blue squares represent all landslide features (types 1, 2, and intermediate). Light brown circles indicate fluidized appearing ejecta. Green diamonds indicate craters hosting pitted materials. Brown diamonds represent depressions and scarps. Green polylines indicate the extent of fractures, grooves, and channels. Purple triangles indicate Floor Fractured Craters (classes 1 and 4). Magenta pentagons represent craters with circumferential fractures. White crosses represent small mounds. Black crosses represent large mounds. The base image is the global Low Altitude Mapping Orbit mosaic (35 m per pixel) courtesy of DLR.

Phillips, 2001; Pilorget & Forget, 2016). Detailed comparison of gully morphology associated with pitted materials on all three bodies may yield insights into the role of specific volatiles in gully development in the future, but this comparison is beyond the scope of our current work.

4. Discussion

Figure 15 shows the global distribution of all features included in our catalog with additional notation for all surface ice exposures identified to date, including permanently shadowed region (PSR) bright deposits with and without spectral confirmation of water ice (Combe et al., 2016, 2018; Ermakov, Mazarico, et al., 2017; Platz et al., 2016). Figure 16 shows the global feature map against the HAMO-based global geologic map developed by Mest et al. (2017). In the global view, features with clear or potential relevance to ice are nearly ubiquitous, consistent with evidence from neutron spectroscopy, ice stability modeling, and gravity and topography analysis, which all indicate that ice is a key constituent of the dwarf planet's crust. Nearly all midlatitude surface ice exposures are proximal to morphological features in our catalog. The abundance of mid- and low-latitude catalog features is notable, as they suggest that subsurface ice is present at latitudes where thermally stable ice is buried too deeply for detection by GRaND (>1 m). Indeed, features in our catalog give us particular insight into low latitude and midlatitude regions, in the depth range of ~100 m to ~20 km where GRaND data and gravity analysis can only provide bulk constraints on composition.

4.1. Evidence for Lateral Heterogeneity

Two global-scale trends are apparent in Figures 15 and 16. The first trend is latitudinal: Type 1 landslides are confined to high latitudes (>70°). Type 2 and intermediate type landslides occur below 70° and throughout the middle and low latitudes. Craters with small-scale features linked to ice (layered and fluidized ejecta, pitted materials, and fractures, grooves, and channels) are also confined to middle and low latitudes. Note

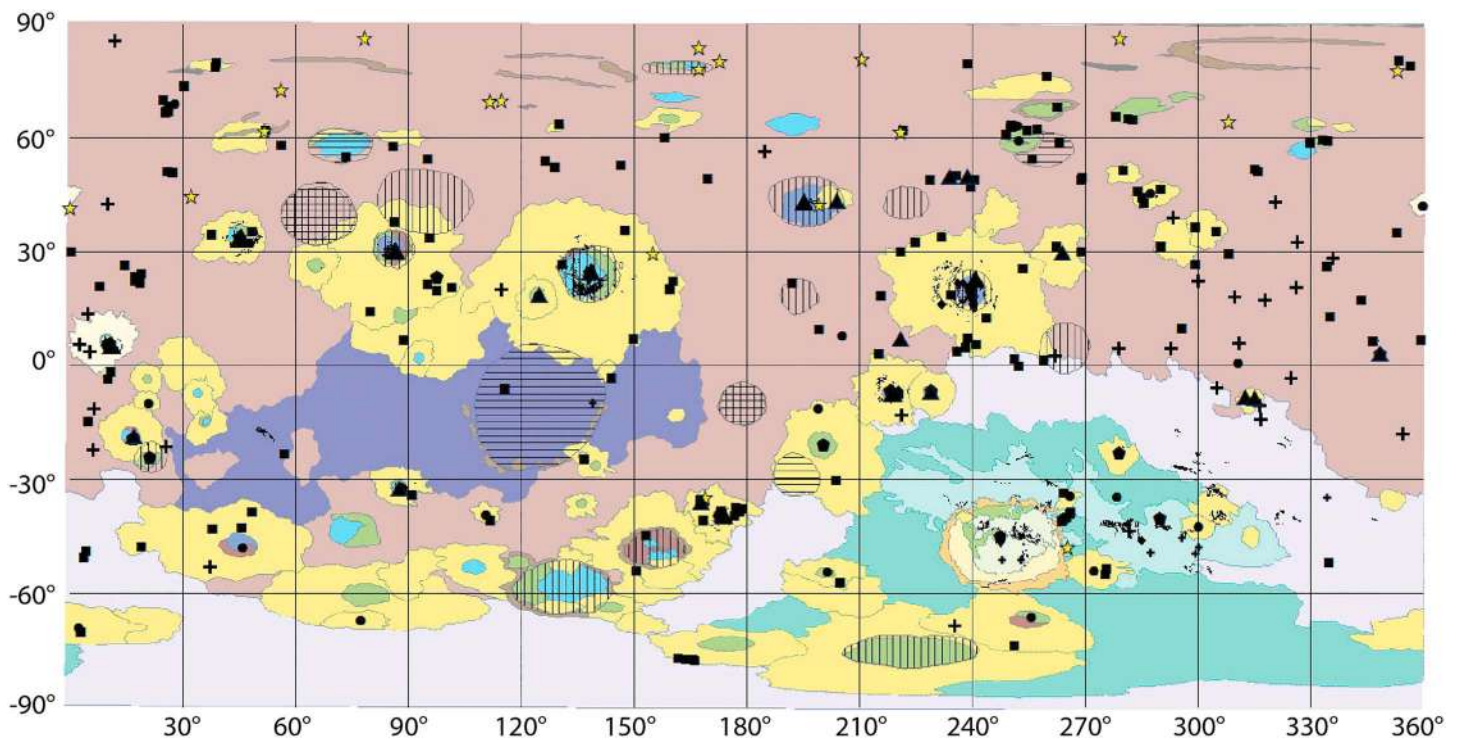


Figure 16. Global view of all cataloged features superposed on the High Altitude Mapping Orbit-based geologic map of Mest et al. (2017). Polygons with horizontal hash marks indicate relaxed craters. Polygons with vertical hash marks indicate central pit craters. Black squares represent all landslide features (types 1, 2, and intermediate). Black circles indicate fluidized appearing ejecta. Large black diamonds indicate craters hosting pitted materials. Small black diamonds represent depressions and scarps. Black polylines indicate the extent of fractures, grooves, and channels. Black triangles indicate Floor Fractured Craters (classes 1 and 4). Black pentagons represent craters with circumferential fractures. Small black crosses represent small mounds. Large black crosses represent large mounds. Yellow stars show surface ice exposures, including Visible and InfraRed Mapping Spectrometer water ice detections (Combe et al., 2018) and permanently shadowed region bright deposits (Platz et al., 2016).

that it is not clear whether the confinement of “interesting” ejecta materials is due to selection bias—that is, the young crater materials on which these features are preserved and can be identified happen to have formed at mid- and low latitudes—or if it is a thermal and/or compositional effect. (See below and section 4.3.) The second trend apparent in Figure 15 is longitudinal. Large domes are primarily confined to the “basin B” region of Ceres’ eastern hemisphere, while a notable dearth of mapped features is apparent to the west of Kerwan crater in the opposite hemisphere. The deficit of morphological evidence for ice over a region of roughly 230,000 km² near Kerwan, along with the clustering of large domes, suggests a first-order hemisphere-scale variation in ice content that may have been driven by ancient impacts, including those that contributed to the formation of Vendimia Planitia and Basins A–C (Marchi et al., 2013). The region lacking in icy features west of Kerwan is itself confined to a latitude range of roughly -30° to 30° , is extensively covered by a smooth geologic unit associated with Kerwan, and hosts a set of degraded parallel grooves or troughs similar to the troughs observed on the floors of Yalode and Urvara craters at its western end.

On shorter length scales, heterogeneity is also apparent. The juxtaposition of large relaxed craters with impact structures of comparable age that exhibit well-preserved topography (e.g., Coniraya and Vinotonus; Figure 2a; Bland et al., 2016) indicates variations in volumetric ice content in the upper 10–30 km from >40 vol. % (ice-dominated rheology) to <35 vol. % (silicate/salt/clathrate dominated rheology) over horizontal distances of tens to hundreds of kilometers. The unique topography of Kerwan crater suggests impacts themselves are a key driver of compositional heterogeneity, with repeat impact heating causing progressive devolatilization of some areas at some depths (Figure 17; Bland, Ermakov, et al., 2018). Impacts also likely play a role in locally enriching shallow ice content, by excavating deep, ice-rich material and depositing it on the surface. Two of the layered-ejecta deposits cataloged in section 3.3 and analyzed by Hughson et al. (2019) occur on the Urvara ejecta blanket. The ejecta materials associated with these two small craters are

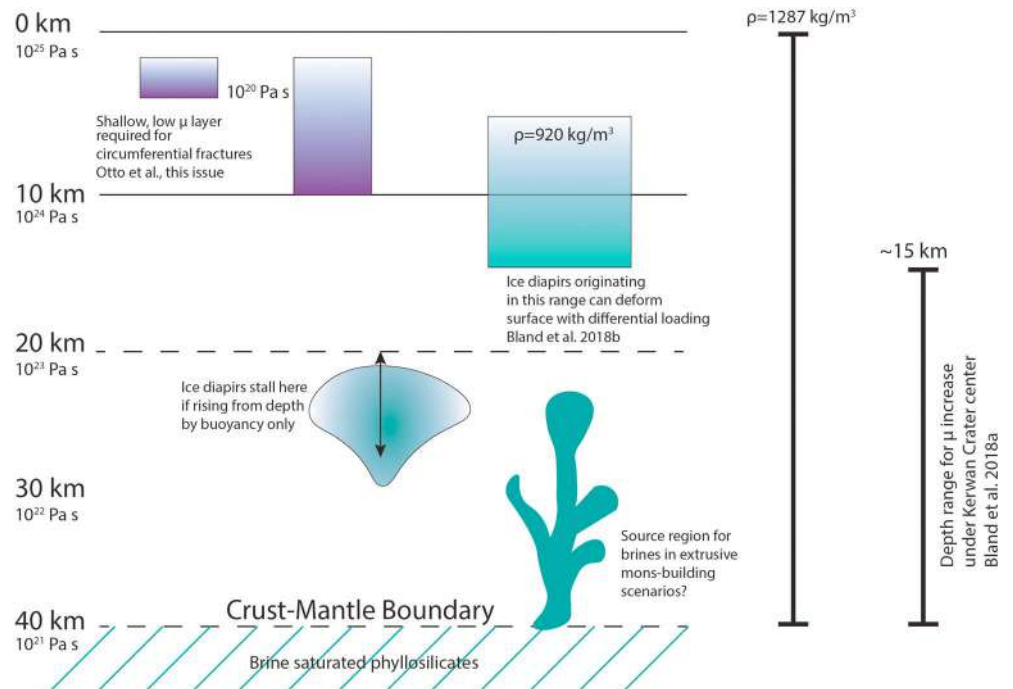


Figure 17. Schematic representation of types of crustal heterogeneity inferred to exist in Ceres' midlatitudes based on analysis of *relaxed craters*, *large domes*, and subtypes of *fractures*, *grooves*, and *channels* (Bland, Sizemore, et al., 2018; Bland et al., 2016; Buczkowski et al., 2018; Otto et al., 2019). Note that the bulk crustal density and the decrease in viscosity with depth were derived by Ermakov, Fu, et al. (2017) based on analysis of global topography. A similar verticle decrease in viscosity was assumed by Bland et al. (2016), Bland, Sizemore, et al. (2018), and by Otto et al. (2019). In their study of diapirism, Bland, Sizemore, et al. (2018) considered by both viscosity and density contrasts with the bulk properties derived by Ermakov, Fu, et al. (2017). Otto et al. (2019) only considered viscosity contrasts.

distinctly asymmetric, with the layered/lobate portions pointing radially toward Urvara. The directionality of these small superposed deposits suggests there may be radial variation in the ice content of the Urvara ejecta blanket, analogous to radial variations in the ice concentration of Martian double-layered crater ejecta inferred from expanded secondaries (Viola et al., 2015).

In their geological mapping of quadrangles Ac-H 13 and Ac-H 14, Crown et al. (2018) noted that the ejecta of Urvara itself exhibits a distinct morphological dichotomy, in which ejecta materials north of approximately -40° are smooth and show extensive evidence of fluidization, while materials south of approximately -40° are rough or hummocky and generally lack evidence of flow. It is unclear if this morphological dichotomy arose due to a preexisting compositional heterogeneity, or if it arose due to differences in average temperature of the preimpact target material and peak temperatures of the resultant ejecta. In either case, the Urvara region exhibits many of the trends of Ceres as a whole in terms of ice-related morphology. Heterogeneity is apparent at length scales ranging from ~ 1 to hundreds of kilometers, and there is an element of latitudinal control poleward of $40\text{--}50^\circ$.

To assess whether these trends are quantitatively significant, we analyzed the distribution of features in our catalog on Ceres' surface using the nearest neighbor statistics. This analysis can assist in geologic interpretation by determining whether a class of features on a sphere is more clustered or more uniformly spaced relative to a random distribution or consistent with a random distribution (Hamilton et al., 2013). For n features, we calculated the distance r from each feature to each other feature. For a particular feature, the smallest value of r is called r_n , which is the "nearest neighbor distance." The mean of the nearest neighbor distances across all n features is r_{av} .

To understand if a set of n features is significantly clustered, uniformly spaced, or neither, we must also calculate r_e , the expected average nearest neighbor distance under the null hypothesis that the features are randomly distributed. We calculated r_e using a Monte Carlo approach. We emplaced n features at random

locations on the Cerean surface and calculated the average nearest neighbor distance. This process was repeated 10,000 times, and the resulting values of r_{av} were averaged to obtain an estimate for r_e . For example, for $n = 63$, we calculated a value of $r_e = 106.4$ km. If $r_{av} < r_e$, the features are relatively clustered, but a statistic is required to test the significance of this result.

The quantity used to test for statistically significant clustering of n features is c (Clark & Evans, 1954), defined as

$$c = \sqrt{\frac{n^2}{A} \left(\frac{r_{av} - r_e}{0.26136} \right)}, \quad (1)$$

where A is the surface area of Ceres; c quantifies the number of standard deviations difference (based on a Poisson random distribution) between r_{av} and r_e . If $c < -2$, we inferred that the distribution of features is significantly more clustered relative to a random distribution. If $c > 2$, we inferred that the distribution of features is significantly more uniform relative to a random distribution. For any other value of c , we interpreted the set of features as not distinguishable from a random distribution with confidence.

We considered the catalog of large domes, relaxed craters, type 1 landslides, and craters with pits, fractures, and grooves. We found a value of $c = -2.42$, indicating that the features are unlikely to be consistent with a random distribution and are more clustered than expected. Caution must be exercised in interpreting this result because the different classes of features are sensitive to ice at different depths and temperatures, but some geological interpretations are suggested. The clustered structure is likely a result of type 1 landslides occurring at high latitudes (Schmidt et al., 2017) but also may be contributed to by a relative dearth of ice near Kerwan or more generally by lateral heterogeneity in ice content.

We note that the pervasive heterogeneity that we infer from morphological analysis occurs at depths greater than tens of meters. Analysis of GRaND data indicates ice concentration is *not* longitudinally variable in the upper decimeters of the surface, perhaps because impact gardening and vapor diffusion act together to homogenize the distribution of ice at very shallow depths. The large footprint of the GRaND instrument also limits the ability to detect variations at lateral length scales less than hundreds of kilometers.

4.2. Evidence for Stratigraphy (Vertical/Radial Heterogeneity)

Three independent lines of evidence suggest there may be pervasive shallow stratigraphy or vertical variations in ice content in the upper few to <20 km of Ceres' crust in the latitude band $\pm 60^\circ$. First, morphological analysis and derivation of flow parameters in type 1 and 2 landslides suggest type 1 landslides occur due to deep failure in a vertically homogeneous substrate (poleward of 70°), while type 2 features arise due to shallow failure in a vertically heterogeneous substrate at lower latitudes. Chilton et al. (2019) argue that this difference reflects the presence of an ice-depleted layer between the ice table (the depth of thermal ice stability; Schorghofer, 2016) and deeper regions of more concentrated ice. They further hypothesize that this ice-depleted layer was produced by successive impacts, that it contains localized lenses of concentrated ice, and that its thickness increases with decreasing latitude.

The second line of evidence for shallow stratigraphy comes from the solid state diapirism hypothesis for large dome formation. Numerical models of the buoyant rise of ice spheres in Ceres' crust show that ice diapirs cannot reach depths shallower than 20 km via buoyancy alone (Bland, Sizemore, et al., 2018). Models that produce uplift comparable to observed dome topography require the presence of a low-density, low-viscosity layer with properties similar to ice at depths of ~ 5 –20 km, along with differential loading caused by crater excavation (Bland, Sizemore, et al., 2018). The same model has been proposed to explain fracture patterns in floor fracture craters (Buczowski et al., 2018). If the diapirism hypothesis remains viable for both types of features (large domes and FFCs), our maps indicate that shallow layering may be pervasive, though patchy over much of the midlatitude and low latitudes of Ceres.

The third independent line of evidence for ice stratigraphy comes from numerical modeling of the stresses responsible for the formation of circumferential fractures (Otto et al., 2019). Modeled stresses are only consistent with the observed fractures if the subsurface contains a low-viscosity (10^{20} Pa s) layer at depths <10 km. The geographic extent of craters with circumferential fractures again suggests that shallow stratigraphy is common throughout the middle and low latitudes, although it is unclear if this stratigraphy is

primarily compositional or arises due to impact heating or both. In all three scenarios, layering is likely to be laterally discontinuous.

Figure 17 shows a schematic summary of vertical variations of material properties that have been inferred from the presence of circumferential fractures, floor fractures, and large domes. The extrusive cryovolcanism hypothesis for large dome development may provide a fourth line of evidence for stratigraphy in Ceres' crust. It is unclear if the liquid brines proposed to have formed Ahuna Mons (Ruesch et al., 2016) and other large domes (Sori et al., 2018) must be sourced from a brine saturated layer in the upper mantle at depths >40 km (Fu et al., 2017), or if they could be sourced from shallower inclusions of melt in the crust at depths more consistent with the diapir model (<20 km). Based on thermal modeling, the second scenario is less plausible. However, silicate diapirism, magmatism, and volcanism commonly occur together on terrestrial worlds. It is not unreasonable to assume the same is true on Ceres, and that ice diapirs and cryomagmas may arise from common or connected reservoirs in the crust and upper mantle. The presence of a large population of domes in the basin B region indicates that the average water content of the crust is enhanced at depths shallower than the ~ 40 -km crust/mantle boundary in this region.

4.3. Selection Biases and the Ambiguity of Low Density Phases

There are two key biases in our searches for ice-related morphological features. First, throughout the primary mission, lighting conditions at polar latitudes ($>70^\circ$) were substantially more favorable to feature identification in the northern hemisphere than in the south. Further, Ceres' low obliquity ensures that identification of small features will always be challenging at high latitude due to shadowing, regardless of season. Second, the majority of small features we identified on Ceres occur on the freshest, smoothest crater materials (Figure 16). Pervasive cratering at all length scales prevents identification of small features over large portions of the surface and appears to degrade pitted materials; fractures, grooves, and channels; lobate landslides and ejecta; and small mounds on short timescales.

Lighting conditions had a major effect on independent searches for surface ice exposures in permanently shadowed regions (Ermakov, Mazarico, et al., 2017; Platz et al., 2016). Only two southern hemisphere candidates have been identified; searches for southern examples will begin during Dawn's second extended mission at Ceres. In contrast, any north/south bias arising from lighting conditions in our catalog of morphological features is probably minor. Lighting differences may have caused us to slightly underrepresent type 1 landslides poleward of -60° . Hemispheric differences in the distribution of lobate landslides versus lobate ejecta occur equatorward of 60° , where detections were not strongly affected by shadows. Similarly, lighting conditions posed challenges to detection of small-scale features such as pitted materials and fractures, grooves, and channels at high latitude but did not obscure the large-scale morphology of craters. The characteristically flat-floored craters that host the pitted materials and fractures, grooves, and channels are absent poleward of 60 – 70° . Finally, if lighting played a role in the nondetection of polygonal patterned ground (section 3.6), both hemispheres were affected equally.

The bias toward feature identification on young terrains is significant in our data set, and it raises interesting questions. First, are small-scale features that are easily degraded (pits, fractures, lobate ejecta, and landslides) produced in nearly all impacts and destroyed, or do some or all of these features develop only under conditions that are spatially and/or temporally constrained? All of the features in our catalog occur in a range of preservation states, suggesting older examples once existed. However, we also observe substantial lateral heterogeneity in the occurrence of lobate and fluidized ejecta, pitted material, landslides, and fractures associated with individual, well-preserved craters (e.g., Ikapati) and morphological differences in craters of comparable size and age (e.g., Ezinu and Gaue). So target heterogeneity has played an important role in the morphology of young craters. The same was likely true in the more distant past, but was similar morphology produced? Complex craters hosting large floor fractures (Class 1 FFCs) and simple craters with interior moats (Class 4 FFCs) appear to be systematically shallower than the general population of Ceres' craters, independent of degradation state (Buczowski et al., 2016, 2018), suggesting that these craters may have characteristics unique to Ceres' recent geologic history (<1 Ga?). In contrast, craters with circumferential fractures (of which the class 1 and 4 FFCs are a subset) are not systematically shallow as a group, although they are systematically young. (At <600 Ma, Yalode is the oldest crater in the group.) Crown et al. (2018) and Otto et al. (2019) have both suggested that Cerean craters may exhibit a unique form of degradation that involves fracturing and collapse of crater rims. These processes combined with floor uplift could

preferentially erase older FFCs, consistent with the observed deficit of large craters on Ceres (Marchi et al., 2016) and the observation of a shallow, heavily degraded Yalode-sized crater at the boundary between the Yalode and Rongo quadrangles (Crown et al., 2018; Platz et al., 2018). Thus, it is unlikely that the FFCs are a unique feature of the epoch in which we are observing Ceres—though it is possible.

The second question raised by the bias toward identification of young features in our catalog concerns the apparent “gap” west of Kerwan: Is the lack of identified features in this region due to a relative deficit of subsurface ice, or a deficit of young craters with well-preserved ejecta? The statistical analysis presented in section 4.1 suggests the observed distribution of features is more clustered than a random distribution, and the presence of the gap may contribute to this result. On morphological grounds, there is reason to believe the subsurface may be abnormally ice-depleted in this region. The gap occurs on part of the extended Kerwan smooth material, one of the oldest and most heavily cratered geologic units on Ceres. One of the few features mapped in this region is a set of degraded Nar-Sulcus-like troughs and grooves, suggesting that the region west of Kerwan may be the floor of an ancient, degraded impact basin. Kerwan itself is thought to have substantially depleted the subsurface of water at depths >15 km (Bland, Ermakov, et al., 2018). Our hypothesized earlier impact to the west could have similarly depleted the deep portions of the crust, while the high temperatures achieved in the ejecta of these two large, equatorial impacts (Marchi et al., 2013) may have led to the deposition of substantially devolatilized material at the surface. Subsequent bombardment by smaller impactors would enhance the regional deficit once it was established.

Our interpretation of the features in our catalog as having a genetic relationship with ice—along with our proposed scenario of early impacts driving large-scale heterogeneities in the modern cryosphere—demands some discussion of the relative abundance and differing stability conditions of water-bearing phases in the crust. As noted in section 3.1, Ceres’ bulk crust likely consists of a three-component mixture of <25 vol. % water ice, $<29\%$ carbonates and phyllosilicates, and $>36\%$ high strength hydrated phases, for example, clathrates and hydrated salts (Ermakov, Fu, et al., 2017; Fu et al., 2017). Based on thermal modeling, Castillo-Rogez et al. (2018) argued that the crust should contain less than 20 vol. % salts, about two thirds of which is hydrohalite ($\text{NaCl} \cdot 2\text{H}_2\text{O}$). The rest is a mixture of anhydrous salts, in particular chlorides, such as the ammonium chloride detected in a few locations on Ceres (Raponi, de Sanctis, Carrozzo, et al., 2018). Hydrated salts are generally more viscous than ice at the same temperature due to the complex structure they develop when crystallizing at the solution eutectic (e.g., McCarthy et al., 2007). They are also denser than ice by up to a factor of 2.5. Thus, at typical subsurface temperatures, hydrated salt lenses are not good candidates for the low viscosity materials invoked in the production of circumferential fractures (Otto et al., 2019) or the low-density materials invoked to explain the formation of large domes by solid state diapirism (Bland, Sizemore, et al., 2018). On the other hand, anhydrous chlorides soften ice at low temperature and can promote significant melting in response to impact induced heating, so the combination of impact heat, salts, and ice is likely critical to the production of many observed morphological features.

The presence of clathrate hydrates adds an additional layer of ambiguity in the composition of the upper kilometers of the crust. At <200 K, CO_2 and CH_4 clathrates are stable at <0.1 MPa (Yasuda & Ohmura, 2008) or roughly 3 km below Ceres’ surface assuming a bulk crustal density of $1,287$ kg/m³. Clathrates are destabilized upon impact; they release their trapped gases, and their constituent H_2O is converted to liquid, vapor, or ice dependent upon local temperature and pressure conditions. Clathrates melt at the same temperature as conventional ice. When entrained in ejecta or destabilized at shallow depth, clathrates will not reform upon refreezing even if there is gas in the system, because pressures are too low (Mousis et al., 2015). Indeed, at elevated temperatures (>200 K), the pressure requirement for clathrate formation increases to ~ 1 MPa or greater (equivalent to depths >200 km). Thus, destabilization of clathrates on impact could play an important role in the production of many of the ejecta characteristics we have attributed broadly to “ice” (e.g., post depositional flow, lobate margins, pitting); shallow clathrates could also provide another path for the heat pulse from an impact to produce the low viscosity layer implicated in the development of circumferential fractures. In general, conventional ice and/or clathrates are the best candidate materials for the low-viscosity and/or low-density layers invoked to explain fracturing and doming in craters. Further, repeat impacts have likely driven a progressive conversion of shallow clathrate hydrate to conventional ice in parallel with a progressive loss of H_2O to space from both sources.

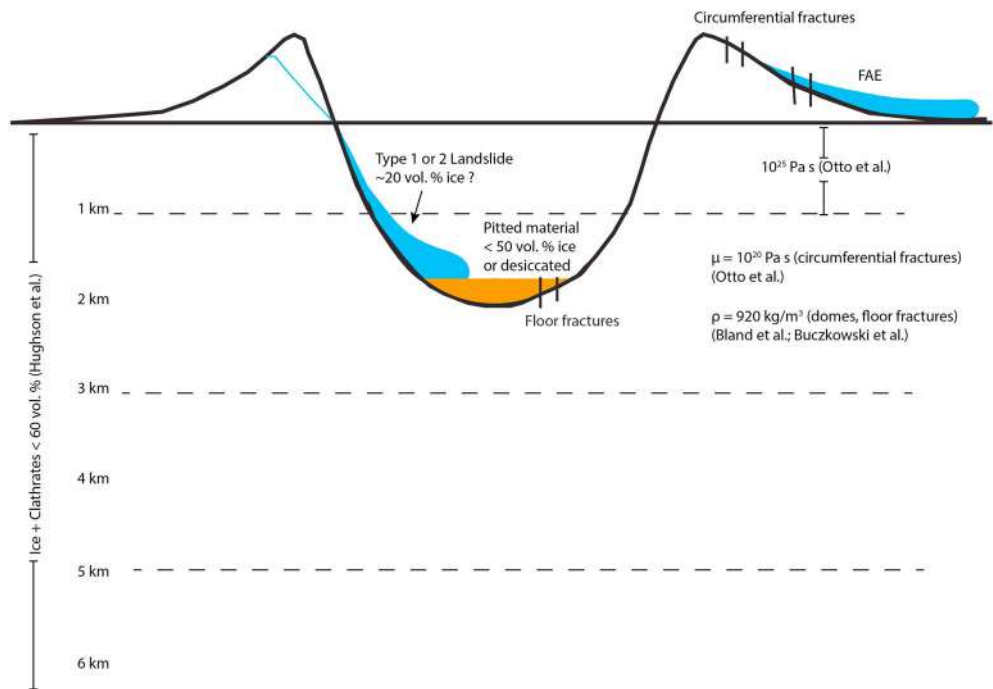


Figure 18. Schematic representation of relative locations of *lobate landslides and ejecta*, *pitted materials*, circumferential fractures and floor fractures, and derived constraints on their material properties and composition. High-resolution imaging of these features could improve our understanding of the ice content of the upper 100 m to 2 km. See discussion in text. FAE = fluidized appearing ejecta.

4.4. Evolution of the Cryosphere and Future Morphological Observations

Our discussion of lateral and vertical heterogeneity in the cryosphere hinges on the role of impacts in the devolatilization of Ceres' crust and the excavation and delivery of ice-rich materials from depth to the near surface. In the broad picture we have painted, Ceres' crust is initially ice rich and globally uniform in composition. Early large impacts remove material and establish large-scale compositional heterogeneity. Subsequent impacts (1) contribute to the depletion of ice in the upper several kilometers, (2) excavate water-rich ejecta from depth, laying down shallow ice-rich layers, and may (3) facilitate cryomagmatic and/or cryovolcanic activity via fracturing, transient melt production, and differential loading of the subsurface due to cavity excavation. Average temperature differences between the equator and the poles cause H₂O loss to occur preferentially at low latitude and midlatitudes, while high latitude ice is more protected, producing a relatively ice-depleted upper layer equatorward of ~60–70°.

Against this backdrop, two key questions emerge: First, are impacts the primary driver of H₂O loss in the current epoch? Second, how much of a role has deep endogenic activity played in the production of putative cryomagmatic and cryovolcanic features? We briefly discuss how future morphological observations might address these questions below.

Interest in contemporary H₂O loss mechanisms from Ceres was piqued by detections of water vapor outgassing by the Herschel Space Observatory when the Dawn spacecraft was still en route from Vesta (Küppers et al., 2014). Explaining the H₂O production rates derived from the Herschel observations was a significant challenge throughout Dawn's mission at Ceres. Theoretical studies of sublimation of ice from the buried ice table (Schorghofer, 2016), of sublimation of ice from surface exposures (Landis et al., 2017), and of sputtering from solar energetic particle events (Villarreal et al., 2017) all failed to produce the Küppers et al. (2014) production rates by orders of magnitude. Reevaluation of the Herschel data may soon bring theoretical and observational production rates into better agreement. At the same time, small impacts and landslides that are not resolved in FC images hold promise to increase theoretical estimates of H₂O production, if they can expose volumetrically dominant ice. High-resolution morphological analysis (during Dawn's second extended mission at Ceres or by future missions) could give important insights into the ice content of the upper ~5 m of the regolith, as well as the viability and relative importance of proposed vapor production

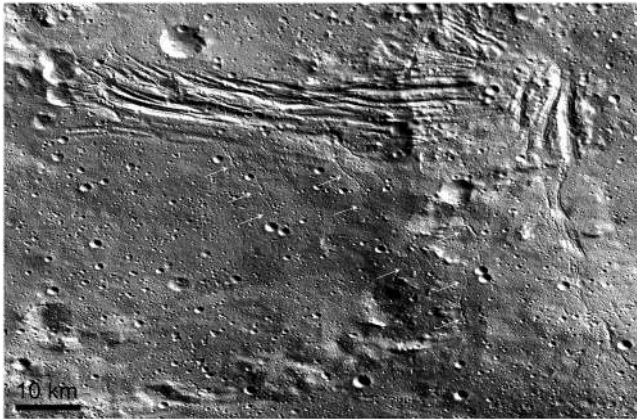


Figure 19. Detail of the Nar sulcus region showing large “troughs” or faults associated with a large dome on the western floor of Yalode crater. Grooves and channels are indicated by white arrows.

mechanisms. Specifically, high resolution images could be used to search for very young ice-exposing craters (diameters <20 m, similar to those exposed in the Martian midlatitudes; Byrne et al., 2009) and make improved estimates of surface sublimation rates based on total number of fresh craters and inferences about the concentration of exposed ice. Identifying locations where near-surface ice might be pore filling or even exceed the pore volume of the regolith would be of particular interest for modeling outgassing rates where ice is exposed by small impacts or landslides.

High-resolution images would also allow for systematic searches for thermal contraction polygons, pits/scarps/dissection, and other small-scale features not resolved in current data sets. These searches could be targeted specifically on locations of identified lobate landslides and ejecta and pitted materials and might better constrain the relative abundance of ice in these features (Figure 18). Identification of small-scale textures on type 1 and 2 landslides in the northern hemisphere and intermediate landslides at Juling crater would be particularly valuable for establishing links

between volumetric ice content of the shallow subsurface and the occurrence of surface ice exposures (Combe et al., 2016, 2018; Platz et al., 2016; Raponi, de Sanctis, Frigeri, et al., 2018). High-resolution imaging might also give insights into what mechanism is most responsible for the pervasive “blurring” of Ceres’ geologic unit boundaries (Crown et al., 2018). Small-scale pits and scarps (<10 m) produced by sublimation or small-scale thermal contraction polygons on Ceres’ smooth materials could explain the generally muted character of the surface. Alternatively and more likely, the dominance of small impact craters may continue to very small spatial scales, with associated heating, transient enhanced sublimation, and turbulent mixing producing the observed muting. Identifying the small-scale textures that give rise to large-scale muting would also test the hypothesis that impact induced mixing, rather than a uniquely low regolith porosity, may account for the shallowness and overall low volumetric concentration of ice detected by GRaND at high latitudes (Prettyman et al., 2017).

High-resolution imaging of targeted locations may also provide insights into the origin of putative cryomagmatic and cryovolcanic features. At Ahuna Mons and Occator crater, high-resolution images could reveal surface textures and/or superposition relationships and constrain ice/brine content of putative cryolavas as well as the timing of their emplacement. Throughout the basin B region, high-resolution imaging would allow for the estimation of ages for different large domes via crater counting. Establishment of relative ages for the individual large domes would allow for direct testing of the hypothesis that the domes form via extrusion and relax on timescales of hundreds of megayears thereafter. Establishment of absolute ages for the individual large domes would allow the timing of their formation (or most recent extrusive event) to be compared directly to global models of thermal evolution. High-resolution images of large domes and craters exhibiting all subtypes of fractures, grooves, and channels might also reveal previously undetected morphological indicators of extrusion. The Nar Sulcus region of Yalode crater is a particularly promising region for this type of analysis, as all three subtypes of fractures, grooves, and channels are collocated there with a large dome (Figure 19). Likewise, the Urvara crater floor contains a local topographic high (not included in our large domes feature class) proximal to all subtypes of fractures, grooves, and channels, one of the better pingo candidates in the small domes feature class, and two regions of smooth material with distinct ages (Crown et al., 2018).

Although more detailed imaging of any or all of the features in our catalog would provide new insights into Ceres’ enigmatic subsurface, we emphasize that future morphological studies would be strongly complemented by the availability of ground penetrating radar and a high-resolution visible and near-infrared spectrometer. Modeling and interpretation of all identified features in our catalog would be improved by more quantitative data relevant to ice content at depths >1 m.

5. Conclusions

We have developed a comprehensive global catalog and maps of the morphological features that have clear or potential relevance to subsurface ice using data acquired during the Dawn spacecraft’s primary and first

extended missions at Ceres. Morphological features linked to ice are nearly ubiquitous on the dwarf planet, consistent with multiple lines of observational evidence that ice is a key component of Ceres' crust. Regional deficits and clusters of features indicate that ice concentration is heterogeneous on nearly all length scales, from hundreds of kilometers to <1 km. Impacts are likely the key driver of heterogeneity, causing progressive devolatilization of the low latitude and midlatitude crust on billion-year timescales but also producing localized enhancements in near-surface ice content via excavation of deep ice-rich material and facilitation of cryomagmatic and cryovolcanic activity. Our analysis indicates that pervasive stratigraphy associated with ice-rich layers is present in the crust today. Impacts may be the dominant mechanism for ice loss on modern Ceres. Our analysis also suggests specific locations where future high-resolution imaging can be used to probe (1) the role of small impacts in driving volatile loss and better constrain current loss rates and (2) the history of putative cryomagmatic and cryovolcanic features. The Cerean cryosphere and its unique morphology promise to be a rich subject of ongoing research for years to come.

Acknowledgments

This research was enabled by the many individuals involved in the successful operations of the Dawn Mission at Ceres, including the NASA Dawn Science and Flight teams at the Jet Propulsion Laboratory (JPL), the instrument teams at the Max Planck Institute for Solar System Research, the German Aerospace Center (DLR), the Italian National Institute for Astrophysics (INAF), and the Planetary Science Institute. The authors also wish to thank Livio Tornabene and an anonymous reviewer whose comments improved the manuscript. This work was supported in part by NASA's Dawn at Ceres Guest Investigator Program. The Dawn mission is led by the University of California, Los Angeles and is managed by JPL under the auspices of the NASA Discovery Program Office. The Dawn data are archived in the NASA Planetary Data System (<http://sbn.psi.edu/pds/archive/dawn.html>).

References

- Alzate, N., & Barlow, N. G. (2011). Central pit craters on Ganymede. *Icarus*, *211*(2), 1274–1283. <https://doi.org/10.1016/j.icarus.2010.10.015>
- Barlow, N. G. (2006). Impact craters in the northern hemisphere of Mars: Layered ejecta and central pit characteristics. *Meteoritics and Planetary Science*, *41*(10), 1425–1436. <https://doi.org/10.1111/j.1945-5100.2006.tb00427.x>
- Barlow, N. G., Boyce, J. M., Costard, F. M., Craddock, R. A., Garvin, J. B., Sakimoto, S. E. H., Kuzmin, R. O., et al. (2000). Standardizing the nomenclature of Martian impact crater ejecta morphologies. *Journal of Geophysical Research*, *105*(E11), 26,733–26,738. <https://doi.org/10.1029/2000JE001258>
- Barlow, N. G., & Tornabene, L. L. (2018). Comparison of central pit craters across the solar system and implications for pit formation models. 49th LPSC, 1687.
- Bland, M. T. (2013). Predicted crater morphologies on Ceres: Probing internal structure and evolution. *Icarus*, *226*(1), 510–521. <https://doi.org/10.1016/j.icarus.2013.05.037>
- Bland, M. T., Ermakov, A. I., Raymond, C. A., Williams, D. A., Bowling, T. J., Preusker, F., et al. (2018). Morphological indicators of a mascon beneath Ceres' largest crater, Kerwan. *Geophysical Research Letters*, *45*, 1297–1304. <https://doi.org/10.1002/2017GL075526>
- Bland, M. T., Raymond, C. A., Schenk, P. M., Fu, R. R., Kneissl, T., Pasckert, J. H., et al. (2016). Composition and structure of the shallow subsurface of Ceres revealed by crater morphology. *Nature Geoscience*, *9*(7), 538–542. <https://doi.org/10.1038/ngeo2743>
- Bland, M. T., Sizemore, H. G., Buczkowski, D. L., Sori, M. M., Raymond, C. A., King, S. D., & Russell, C. T. (2018). Why is Ceres lumpy? Surface deformation induced by solid-state subsurface flow. 49th LPSC, 1627.
- Blewett, D. T., Chabot, N. L., Denevi, B. W., Ernst, C. M., Head, J. W., Izenberg, N. R., et al. (2011). Hollows on Mercury: MESSENGER evidence for geologically recent volatile-related activity. *Science*, *333*(6051), 1856–1859. <https://doi.org/10.1126/science.1211681>
- Bowling, T. J., Ciesla, F. J., Davison, T. M., Scully, J. E. C., Castillo-Rogez, J. C., Marchi, S., & Johnson, B. C. (2018). Post-impact thermal structure and cooling timescales of Occator crater on asteroid 1 Ceres. *Icarus*.
- Bowling, T. J., Ciesla, F. J., Marchi, S., Davison, T. M., Castillo-Rogez, J. C., De Sanctis, M. C., et al. (2016). Impact induced heating of Occator crater on asteroid 1 Ceres. 47th LPSC, 2268.
- Boyce, J. M., Mouginiis-Mark, P., & Robinson, M. (2016). An LROC update: The Tsiolkovsky landslide. 47th LPSC, 2471.
- Boyce, J. M., Wilson, L., Mouginiis-Mark, P. J., Hamilton, C. W., & Tornabene, L. L. (2012). Origin of small pits in Martian impact craters. *Icarus*, *221*(1), 262–275. <https://doi.org/10.1016/j.icarus.2012.07.027>
- Boynton, W. V., Feldman, W. C., Squyres, S. W., Prettyman, T. H., Bruckner, J., Evans, L. G., et al. (2002). Distribution of hydrogen in the near surface of Mars: Evidence for subsurface ice deposits. *Science*, *297*(5578), 81–85. <https://doi.org/10.1126/science.1073722>
- Bray, V., Schenk, P., Melosh, H. J., Morgan, J., & Collins, G. (2012). Ganymede crater dimensions—Implications for central peak and central pit formation and development. *Icarus*, *217*(1), 115–129. <https://doi.org/10.1016/j.icarus.2011.10.004>
- Bray, V. J., Tornabene, L. L., Keszthelyi, L. P., McEwen, A. S., Hawke, B. R., Giguere, T. A., et al. (2010). New insight into lunar impact melt mobility for the LRO camera. *Geophysical Research Letters*, *37*, L21202. <https://doi.org/10.1029/2010GL044666>
- Buczkowski, D. L., Schmidt, B. E., Williams, D. A., Mest, S. C., Scully, J. E. C., Ermakov, A. I., et al. (2016). The geomorphology of Ceres. *Science*, *353*(6303), aaf4332. <https://doi.org/10.1126/science.aaf4332>
- Buczkowski, D. L., Sizemore, H. G., Bland, M. T., Scully, J. E. C., Quick, L. C., Hughson, K. H. G., et al. (2018). Floor-fractured craters on Ceres and implications for interior processes. *Journal of Geophysical Research: Planets*, *123*, 3188–3204. <https://doi.org/10.1029/2018JE005632>
- Byrne, S., Dundas, C. M., Kennedy, M. R., Mellon, M. T., McEwen, A. S., Cull, S. C., et al. (2009). Distribution of mid-latitude ground ice on Mars from new impact craters. *Science*, *325*(5948), 1674–1676. <https://doi.org/10.1126/science.1175307>
- Byrne, S., & Ingersoll, A. P. (2003). Martian climatic events on timescales of centuries: Evidence from feature morphology in the residual south polar ice cap. *Geophysical Research Letters*, *30*(13), 1696. <https://doi.org/10.1029/2003GL017597>
- Castillo-Rogez, J. C., & McCord, T. B. (2010). Ceres' evolution and present state constrained by shape data. *Icarus*, *205*(2), 443–459. <https://doi.org/10.1016/j.icarus.2009.04.008>
- Castillo-Rogez, J. C., Neveu, M., McSween, H. Y., Fu, R., Toplis, M., & Prettyman, T. (2018). Insights into Ceres' evolution from surface composition. *Meteoritics and Planetary Science*, *53*(9), 1820–1843. <https://doi.org/10.1111/maps.13181>
- Chilton, H. T., Schmidt, B. E., Duarte, K., Ferrier, K. L., Hughson, K. H. G., Scully, J. E. C., et al. (2019). Landslides on Ceres: Inferences into ice content and layering in the upper crust. *Journal of Geophysical Research: Planets*, *124*. <https://doi.org/10.1029/2018JE005634>
- Clark, P. J., & Evans, F. C. (1954). Distance to nearest neighbor as a measure of spatial relationships in populations. *Ecology*, *35*(4), 445–453. <https://doi.org/10.2307/1931034>
- Combe, J. P., McCord, T. B., Tosi, F., Ammannito, E., Carrozzo, F. G., de Sanctis, M. C., et al. (2016). Detection of local H₂O exposed at the surface of Ceres. *Science*, *353*(6303), aaf3010. <https://doi.org/10.1126/science.aaf3010>
- Combe, J. P., Raponi, A., Tosi, F., de Sanctis, M. C., Carrozzo, F. G., Zambon, F., et al. (2018). Exposed H₂O-rich areas detected on Ceres with the Dawn visible and infrared mapping spectrometer. *Icarus*, *318*, 22–41. <https://doi.org/10.1016/j.icarus.2017.12.008>
- Croft, S. (1983). A proposed origin for palimpsests and anomalous pit craters on Ganymede and Callisto. Proc. Lunar Planet. Sci. Conf., 14th, Part I, J. Geophys. Res., 88, suppl., B71-B89.

- Crown, D. A., Sizemore, H. G., Yingst, R. A., Mest, S. C., Platz, T., Berman, D. C., et al. (2018). Geologic mapping of the Urvara and Yalode quadrangles of Ceres. *Icarus*, *316*, 167–190. <https://doi.org/10.1016/j.icarus.2017.08.004>
- Culha, C., & Manga, M. (2016). Geometry and spatial distribution of lenticulae on Europa. *Icarus*, *271*, 49–56. <https://doi.org/10.1016/j.icarus.2015.12.052>
- Cutts, J. A., Soderblom, L. A., Sharp, R. P., Smith, B. A., & Murray, B. C. (1971). The surface of Mars 3. Light and dark markings. *Journal of Geophysical Research*, *76*(2), 343–356. <https://doi.org/10.1029/JB076i002p00343>
- Denevi, B. W., Blewett, D. T., Buczkowski, D. L., Capaccioni, F., Capria, M. T., de Sanctis, M. C., et al. (2012). Pitted terrain on Vesta and implications for the presence of volatiles. *Science*, *338*(6104), 246–249. <https://doi.org/10.1126/science.1225374>
- Dickson, J. L., Head, J. W., & Kreslavsky, M. (2007). Martian gullies in the southern mid-latitudes of Mars: Evidence for climate-controlled formation of young fluvial features based upon local and global topography. *Icarus*, *188*(2), 315–323. <https://doi.org/10.1016/j.icarus.2006.11.020>
- Diniega, S., Hansen, C. J., McElwaine, J. N., Hugenholtz, C. H., Dundas, C. M., McEwen, A. S., & Bourke, M. C. (2013). A new dry hypothesis for the formation of Martian linear gullies. *Icarus*, *225*(1), 526–537. <https://doi.org/10.1016/j.icarus.2013.04.006>
- Dombard, A. J., & Gillis, J. J. (2001). Testing the viability of topographic relaxation as a mechanism for the formation of lunar floor-fractured craters. *Journal of Geophysical Research*, *106*(E11), 27,901–27,909. <https://doi.org/10.1029/2000JE001388>
- Dombard, A. J., & Schenk, P. M. (2013). The giant cue ball: Efficient relaxation of Ceres' craters. 44th LPSC, 1798.
- Duarte, K. D., Schmidt, B. E., Chilton, H. T., Hughson, K. H. G., Sizemore, H. G., Scully, J. E. C., et al. (2019). Landslides on Ceres: Diversity and geologic context. *Journal of Geophysical Research: Planets*. <https://doi.org/10.1029/2018JE005673>
- Dundas, C. M., & McEwen, A. S. (2010). An assessment of evidence for pingos on Mars using HiRISE. *Icarus*, *205*(1), 244–258. <https://doi.org/10.1016/j.icarus.2009.02.020>
- Dundas, C. M., McEwen, A. S., Diniega, S., & Byrne, S. (2010). New and recent gully activity on Mars as seen by HiRISE. *Geophysical Research Letters*, *37*, L07202. <https://doi.org/10.1029/2009GL041351>
- Ermakov, A. I., Fu, R. R., Castillo-Rogez, J. C., Raymond, C. A., Park, R. S., Preusker, F., et al. (2017). Constraints on Ceres' internal structure and evolution from its shape and gravity measured by the Dawn spacecraft. *Journal of Geophysical Research: Planets*, *122*, 2267–2293. <https://doi.org/10.1002/2017JE005302>
- Ermakov, A. I., Mazarico, E., Schröder, S. E., Carsenty, U., Schorghofer, N., Preusker, F., et al. (2017). Ceres's obliquity history and its implications for the permanently shadowed regions. *Geophysical Research Letters*, *44*, 2652–2661. <https://doi.org/10.1002/2016GL072250>
- Fagents, S. A. (2003). Considerations for effusive cryovolcanism on Europa: The post-Galileo perspective. *Journal of Geophysical Research*, *108*(E12), 5139. <https://doi.org/10.1029/2003JE002128>
- Fanale, F. P., & Salvail, J. R. (1989). The water regime of asteroid (1) Ceres. *Icarus*, *82*(1), 97–110. [https://doi.org/10.1016/0019-1035\(89\)90026-2](https://doi.org/10.1016/0019-1035(89)90026-2)
- Fu, R. R., Ermakov, A. I., Marchi, S., Castillo-Rogez, J. C., Raymond, C. A., Hager, B. H., Zuber, M. T., et al. (2017). The interior structure of Ceres as revealed by surface topography. *Earth and Planetary Science Letters*, *476*, 153–164. <https://doi.org/10.1016/j.epsl.2017.07.053>
- Giese, B., Denk, T., Neukum, G., Roatsch, T., Helfenstein, P., Thomas, P. C., et al. (2008). The topography of Iapetus' leading side. *Icarus*, *193*(2), 359–371. <https://doi.org/10.1016/j.icarus.2007.06.005>
- Hamilton, C. W., Beggan, C. D., Still, S., Beuthe, M., Lopes, R. M. C., Williams, D. A., et al. (2013). Spatial distribution of volcanoes on Io: Implications for tidal heating and magma ascent. *Earth and Planetary Science Letters*, *361*, 272–286. <https://doi.org/10.1016/j.epsl.2012.10.032>
- Hesse, M. A., & Castillo-Rogez, J. C. (2018). Longevity of the cryomagma chamber beneath Occator crater on Ceres. 49th LPSC, 1679.
- Hiesinger, H., Marchi, S., Schmedemann, N., Schenk, P., Pasckert, J. H., Neesemann, A., et al. (2016). Cratering on Ceres: Implications for its crust and evolution. *Science*, *353*(6303), aaf4759. <https://doi.org/10.1126/science.aaf4759>
- Hughson, K. H. G., Russell, C. T., Schmidt, B. E., Chilton, H. T., Sizemore, H. G., Schenk, P. M., & Raymond, C. A. (2019). Fluidized appearing ejecta on Ceres: Implications for its near-surface mechanical properties, frictional properties, and composition. *Journal of Geophysical Research: Planets*, *124*. <https://doi.org/10.1029/2018JE005666>
- Hughson, K. H. G., Russell, C. T., Williams, D. A., Buczkowski, D. L., Mest, S. C., Pasckert, J. H., et al. (2018). The Ac-H-5 (Fejokoo) quadrangle of Ceres: Geologic map and geomorphological evidence for ground ice mediated surface processes. *Icarus* <https://doi.org/10.1016/j.icarus.2017.09.035>, *316*, 63–83.
- Kargel, J. S. (1991). Brine volcanism and the interior structures of asteroids and icy satellites. *Icarus*, *94*(2), 368–390. [https://doi.org/10.1016/0019-1035\(91\)90235-L](https://doi.org/10.1016/0019-1035(91)90235-L)
- Kargel, J. S., & Lunine, J. I. (1998). Clathrate hydrates on Earth and in the Solar System. In B. Schmitt, C. de Bergh, & M. Festou (Eds.), *Solar System ices, Astrophysics and Space Science Library* (Vol. 227, pp. 3–32). Dordrecht: Springer. https://doi.org/10.1007/978-94-011-5252-5_5
- Küppers, M., O'Rourke, L., Bockelée-Morvan, D., Zakharov, V., Lee, S., von Allmen, P., et al. (2014). Localized sources of water vapour on the dwarf planet (1) Ceres. *Nature*, *505*(7484), 525–527. <https://doi.org/10.1038/nature12918>
- Landis, M. E., Byrne, S., Schörghofer, N., Schmidt, B. E., Hayne, P. O., Castillo-Rogez, J., et al. (2017). Conditions for sublimating water ice to supply Ceres' exosphere. *Journal of Geophysical Research: Planets*, *122*, 1984–1995. <https://doi.org/10.1002/2017JE005335>
- Lopes, R. M. C., Kirk, R. L., Mitchell, K. L., LeGall, A., Barnes, J. W., Hayes, A., et al. (2013). Cryovolcanism on Titan: New results from Cassini RADAR and VIMS. *Journal of Geophysical Research: Planets*, *118*, 416–435. <https://doi.org/10.1002/jgrg.20062>
- Malin, M. C., Caplinger, M. A., & Davis, S. D. (2001). Observational evidence for an active surface reservoir of solid carbon dioxide on Mars. *Science*, *294*(5549), 2146–2148. <https://doi.org/10.1126/science.1066416>
- Malin, M. C., & Edgett, K. S. (2000). Evidence for recent groundwater seepage and surface runoff on Mars. *Science*, *288*(5475), 2330–2335. <https://doi.org/10.1126/science.288.5475.2330>
- Mangold, N. (2005). High latitude patterned grounds on Mars: Classification, distribution and climatic control. *Icarus*, *174*(2), 336–359. <https://doi.org/10.1016/j.icarus.2004.07.030>
- Mangold, N. (2011). Ice sublimation as a geomorphic process: A planetary perspective. *Geomorphology*, *126*(1–2), 1–17. <https://doi.org/10.1016/j.geomorph.2010.11.009>
- Marchant, D. R., Lewis, A. R., Phillips, W. M., Moore, E. J., Souchez, R. A., Denton, G. H., et al. (2002). Formation of patterned ground and sublimation till over Miocene glacier ice in Beacon Valley, southern Victoria Land, Antarctica. *GSA Bulletin*, *114*(6), 718–730. [https://doi.org/10.1130/0016-7606\(2002\)114<0718:FOPGAS>2.0.CO;2](https://doi.org/10.1130/0016-7606(2002)114<0718:FOPGAS>2.0.CO;2)
- Marchi, S., Bottke, W. F., Cohen, B. A., Wünnemann, K., Kring, D. A., McSween, H. Y., et al. (2013). High-velocity collisions from the lunar cataclysm recorded in asteroidal meteorites. *Nature Geoscience*, *6*(4), 303–307. <https://doi.org/10.1038/ngeo1769>

- Marchi, S., Ermakov, A. I., Raymond, C. A., Fu, R. R., O'Brien, D. P., Bland, M. T., et al. (2016). The missing large impact craters on Ceres. *Nature Communications*, 7(1), 12257. <https://doi.org/10.1038/ncomms12257>
- McCarthy, C. M., Cooper, R. F., Kirby, S. H., Rieck, K. D., & Stern, L. A. (2007). Solidification and microstructures of binary ice-I/hydrate eutectic aggregates. *American Mineralogist*, 92(10), 1550–1560. <https://doi.org/10.2138/am.2007.2435>
- McCord, T. B., & Sotin, C. (2005). Ceres: Evolution and current state. *Journal of Geophysical Research*, 110, E05009. <https://doi.org/10.1029/2004JE002244>
- McCoy, T. J., Sims, M., Schmidt, M. E., Edwards, L., Tornabene, L. L., Crumpler, L. S., et al. (2008). Structure, stratigraphy, and origin of Husband Hill, Columbia Hills, Guseve Crater, Mars. *Journal of Geophysical Research*, 113, E06S03. <https://doi.org/10.1029/2007JE003041>
- Mellon, M. T., Boynton, W. V., Feldman, W. C., Arvidson, R. E., Titus, T. N., Bandfield, J. L., et al. (2008). A prelanding assessment of the ice table depth and ground ice characteristics in Martian permafrost at the Phoenix landing site. *Journal of Geophysical Research*, 113, E00A25. <https://doi.org/10.1029/2007JE003067>
- Mellon, M. T., Jakosky, B. M., & Postawko, S. E. (1997). The persistence of equatorial ground ice on Mars. *Journal of Geophysical Research*, 102(E8), 19,357–19,369. <https://doi.org/10.1029/97JE01346>
- Mellon, M. T., & Phillips, R. J. (2001). Recent gullies on Mars and the source of liquid water. *Journal of Geophysical Research*, 106(E10), 23,165–23,179. <https://doi.org/10.1029/2000JE001424>
- Melosh, H. J. (1982). A schematic model of crater modification by gravity. *Journal of Geophysical Research*, 87(B1), 371–380. <https://doi.org/10.1029/JB087iB01p00371>
- Mest, S. C., Crwon, D. A., Yingst, R. A., Berman, D. C., Williams, D. A., Buczkowski, D. L., et al. (2017). The global geologic map of Ceres based on Dawn HAMO observations. 48th LPSC, 2512.
- Milliken, R. E., & Mustard, J. F. (2003). Erosional morphologies and characteristics of latitude-dependent surface mantles on Mars. Sixth international conference on Mars, 3240.
- Moore, J. M., McKinnon, W. B., Spencer, J. R., Howard, A. D., Schenk, P. M., Beyer, R. A., et al. (2016). The geology of Pluto and Charon through the eyes of new horizons. *Science*, 351(6279), 1284–1293. <https://doi.org/10.1126/science.aad7055>
- Moore, J. M., Mellon, M. T., & Zent, A. P. (1996). Mass wasting and ground collapse in terrains of volatile-rich deposits as a solar system-wide geological process: The pre-Galileo view. *Icarus*, 122(1), 63–78. <https://doi.org/10.1006/icar.1996.0109>
- Mousis, O., Chassefière, E., Holm, N. G., Bouquet, A., Waite, J. H., Geppert, W. D., et al. (2015). Methane clathrates in the Solar System. *Astrobiology*, 15(4), 308–326. <https://doi.org/10.1089/ast.2014.1189>
- Mustard, J. F., Cooper, C. D., & Rifkin, M. K. (2001). Evidence for recent climate change on Mars from the identification of youthful near-surface ground ice. *Nature*, 412(6845), 411–414. <https://doi.org/10.1038/35086515>
- Neveu, M., & Desch, S. J. (2015). Geochemistry, thermal evolution, and cryovolcanism on Ceres with a muddy ice mantle. *Geophysical Research Letters*, 42, 10,197–10,206. <https://doi.org/10.1002/2015GL066375>
- Nuhn, A. M. (2014). Morphologic and structural mapping of layered central uplifts on Mars. *Electronic Thesis and Dissertation Repository*, 2125. Retrieved from <https://ir.lib.uwo.ca/etd/2125>
- Otto, K. A., Marchi, S., Trowbridge, A., Melosh, H. J., & Sizemore, H. G. (2019). Ceres crater degradation inferred from circumferential fracturing. *Journal of Geophysical Research: Planets*, 124. <https://doi.org/10.1029/2018JE005660>
- Pappalardo, R. T., & Barr, A. C. (2004). The origin of domes on Europa: The role of thermal induced compositional diapirism. *Geophysical Research Letters*, 31, L01701. <https://doi.org/10.1029/2003GL019202>
- Pappalardo, R. T., Belton, M. J. S., Breneman, H. H., Carr, M. H., Chapman, C. R., Collins, G. C., et al. (1999). Does Europa have a subsurface ocean? Evaluation of the geological evidence. *Journal of Geophysical Research*, 104(E10), 24,015–24,055. <https://doi.org/10.1029/1998JE000628>
- Pappalardo, R. T., Head, J. W., Greeley, R., Sullivan, R. J., Pilcher, C., Schubert, G., et al. (1998). Geological evidence for solid-state convection in Europa's ice shell. *Nature*, 391(6665), 365–368. <https://doi.org/10.1038/34862>
- Passey, Q. R., & Shoemaker, E. M. (1982). Craters and basins on Ganymede and Callisto: Morphological indicators of crustal evolution. In D. Morrison (Ed.), *Satellites of Jupiter* (pp. 340–378). Tucson: University of Arizona Press.
- Pilorget, C., & Forget, F. (2016). Formation of gullies on Mars by debris flows triggered by CO₂ sublimation. *Nature Geoscience*, 9(1), 65–69. <https://doi.org/10.1038/ngeo2619>
- Platz, T., Nathues, A., Schorghofer, N., Preusker, F., Mazarico, E., Schröder, S. E., et al. (2016). Surface water-ice deposits in the northern shadowed regions of Ceres. *Nature Astronomy*, 1(1), 0007. <https://doi.org/10.1038/s41550-016-0007>
- Platz, T., Nathues, A., Sizemore, H. G., Crown, D. A., Hoffmann, M., Schäfer, M., et al. (2018). Geological mapping of the Ac-10 Rongo quadrangle of Ceres. *Icarus*, 316, 140–153. <https://doi.org/10.1016/j.icarus.2017.08.001>
- Prettyman, T. H., Feldman, W. C., Mellon, M. T., McKinney, G. W., Boyton, W. V., Karunatillake, S., et al. (2004). Composition and structure of the Martian surface at high southern latitudes from neutron spectroscopy. *Journal of Geophysical Research*, 109, E05001. <https://doi.org/10.1029/2003JE002139>
- Prettyman, T. H., Yamashita, N., Toplis, M. J., McSween, H. Y., Schorghofer, N., Marchi, S., et al. (2017). Extensive water ice within Ceres' aqueously altered regolith: Evidence from nuclear spectroscopy. *Science*, 355(6320), 55–59. <https://doi.org/10.1126/science.aah6765>
- Quick, L. C., Buczkowski, D. L., Scully, J. E. C., Ruesch, O., Castillo-Rogez, J., Raymond, C. A., et al. (2018). Thermal and compositional evolution of a brine reservoir beneath Ceres' Occator crater: Implications for cryovolcanism at the surface. 49th LPSC, 2921.
- Quick, L. C., Glaze, L. S., & Baloga, S. M. (2017). Cryovolcanic emplacement of domes on Europa. *Icarus*, 284, 477–488. <https://doi.org/10.1016/j.icarus.2016.06.029>
- Raponi, A., de Sanctis, M. C., Carozzo, F. G., Ciarniello, M., Castillo-Rogez, J. C., Ammannito, E., et al. (2018). Mineralogy of Occator crater on Ceres and insight into its evolution from the properties of carbonates, phyllosilicates, and chlorides. *Icarus*. <https://doi.org/10.1016/j.icarus.2018.02.001>
- Raponi, A., de Sanctis, M. C., Frigeri, A., Ammannito, E., Ciarniello, M., Formisano, M., et al. (2018). Variations in the amount of water ice on Ceres' surface suggest a seasonal water cycle. *Science*, 4(3). <https://doi.org/10.1126/sciadv.aao3757>
- Ruesch, O., Platz, T., Schenk, P., McFadden, L. A., Castillo-Rogez, J. C., Quick, L. C., et al. (2016). Cryovolcanism on Ceres. *Science*, 353(6303), aaf4286. <https://doi.org/10.1126/science.aaf4286>
- de Sanctis, M. C., Raponi, A., Ammannito, E., Ciarniello, M., Toplis, M. J., McSween, H. Y., et al. (2016). Bright carbonate deposits as evidence of aqueous alteration on (1) Ceres. *Nature*, 536(7614), 54–57. <https://doi.org/10.1038/nature18290>
- Schenk, P., Chapman, C., Zahnle, K., & Moore, J. (2004). Ages and interiors: The cratering record of the Galilean Satellites. In *Jupiter* (pp. 427–456). Cambridge, UK: Cambridge University Press.

- Schenk, P., Marchi, S., O'Brien, D., Otto, K., Jaumann, R., Williams, D., et al. (2015). Impact craters on Ceres: Evidence for water-ice mantle? *EPSC*, 10, EPSC2015-400.
- Schenk, P., Marchi, S., O'Brien, D.P., Bland, M., Platz, T., Hoogenboom, T., et al. (2016). Impact cratering on the small planets Ceres and Vesta: S-C transitions, central pits, and the origin of bright spots. 47th LPSC, 1903.
- Schenk, P., Sizemore, H. G., Schmidt, B., Castillo-Rogez, J., De Sanctis, M., Bowling, T., et al. (2018). The central pit and dome at Cerealia Facula bright eposit and floor deposits in Occator crater, Ceres: Morphology, Comparisons and Formation. *Icarus*. <https://doi.org/10.1016/j.icarus.2018.08.010>
- Schenk, P. M. (1993). Central pit and dome craters: Exposing the interiors of Ganymede and Callisto. *Journal of Geophysical Research*, 98(E4), 7475–7498. <https://doi.org/10.1029/93JE00176>
- Schmidt, B. E., Blankenship, D. D., Patterson, G. W., & Schenk, P. M. (2011). Active formation of 'chaos terrain' over shallow subsurface water on Europa. *Nature*, 479(7374), 502–505. <https://doi.org/10.1038/nature10608>
- Schmidt, B. E., Hughson, K. H. G., Chilton, H. T., Scully, J. E. C., Platz, T., Nathues, A., et al. (2017). Geomorphological evidence for ground ice on dwarf planet Ceres. *Nature Geoscience*, 10(5), 338–343. <https://doi.org/10.1038/ngeo2936>
- Schon, S. C., Head, J. W., & Milliken, R. E. (2009). A recent ice age on Mars: Evidence for climate oscillations from regional layering in mid-latitude mantling deposits. *Geophysical Research Letters*, 36, L15202. <https://doi.org/10.1029/2009GL038554>
- Schorghofer, N. (2008). The lifetime of ice on main belt asteroids. *The Astrophysical Journal*, 682(1), 697. <https://doi.org/10.1086/588633-705>
- Schorghofer, N. (2016). Predictions of depth-to-ice on asteroids based on an asynchronous model of temperature, impact stirring, and ice loss. *Icarus*, 276, 88–95. <https://doi.org/10.1016/j.icarus.2016.04.037>
- Schultz, P. M. (1976). Floor-fractured lunar craters. *The Moon*, 15(3-4), 241–273. <https://doi.org/10.1007/BF00562240>
- Scully, J. E. C., Buczkowski, D. L., Raymond, C. A., Bowling, T., Williams, D. A., Neesemann, A., et al. (2018). Ceres' Occator crater and its faculae explored through geologic mapping. *Icarus*. <https://doi.org/10.1016/j.icarus.2018.04.014>
- Scully, J. E. C., Russell, C. T., Castillo-Rogez, J. C., Raymond, C. A., & Ermakov, A. I. (2018). Introduction to the special issue: The formation and evolution of Ceres' Occator crater. *Icarus*. <https://doi.org/10.1016/j.icarus.2018.02.029>
- Scully, J. E. C., Russell, C. T., Yin, A., Jaumann, R., Carey, E., Castillo-Rogez, J., et al. (2015). Geomorphological evidence for transient water flow on Vesta. *Earth and Planetary Science Letters*, 411, 151–163. <https://doi.org/10.1016/j.epsl.2014.12.004>
- Searls, M. L., Mellon, M. T., Mustard, J. F., Milliken, R. E., Martinez-Alonso, S., & HiRISE Team (2007). Mid-latitude dissected mantle terrain as viewed from HiRISE. Seventh international conference on Mars, 3351.
- Senft, L. E., & Steward, S. T. (2011). Modeling the morphological diversity of impact craters on icy satellites. *Icarus*, 214(1), 67–81. <https://doi.org/10.1016/j.icarus.2011.04.015>
- Sharp, R. P., Murray, B. C., Leighton, R. B., Soderblom, L. A., & Cutts, J. A. (1971). The surface of Mars 4. South polar cap. *Journal of Geophysical Research*, 76(2), 357–368. <https://doi.org/10.1029/JB076i002p00357>
- Sizemore, H. G., & Mellon, M. T. (2008). Laboratory characterization of the structural properties controlling dynamical gas transport in Mars-analog soils. *Icarus*, 197(2), 606–620. <https://doi.org/10.1016/j.icarus.2008.05.013>
- Sizemore, H. G., Platz, T., Schorghofer, N., Prettyman, T. H., de Sanctis, M. C., Crown, D. A., et al. (2017). Pitted terrains on (1) Ceres and Implications for shallow subsurface volatile distribution. *Geophysical Research Letters*, 44, 6570–6578. <https://doi.org/10.1002/2017GL073970>
- Soderblom, L. A., Kreidler, T. J., & Masursky, H. (1973). Latitudinal distribution of a debris mantle on the Martian surface. *Journal of Geophysical Research*, 78(20), 4117–4122. <https://doi.org/10.1029/JB078i020p04117>
- Soderblom, L. A., Malin, M. C., Cutts, J. A., & Murray, B. C. (1973). Mariner 9 observations of the surface of Mars in the north polar region. *Journal of Geophysical Research*, 78(20), 4197–4210. <https://doi.org/10.1029/JB078i020p04197>
- Sori, M. M., Byrne, S., Bland, M. T., Bramson, A. M., Ermakov, A. I., Hamilton, C. W., et al. (2017). The vanishing cryovolcanoes of Ceres. *Geophysical Research Letters*, 44, 1243–1250. <https://doi.org/10.1002/2016GL072319>
- Sori, M. M., Sizemore, H. G., Byrne, S., Bramson, A. M., Bland, M. T., Stein, N. T., & Russell, C. T. (2018). Ceres' Cryovolcanic rates on Ceres revealed by topography. *Nature Astronomy*, 2(12), 946–950. <https://doi.org/10.1038/s41550-018-0574-1>
- Tornabene, L. L., Osinski, G. R., McEwen, A. S., Boyce, J. M., Bray, V. J., Caudill, C. M., et al. (2012). Widespread crater-related pitted materials on Mars: Further evidence for the role of target volatiles during the impact process. *Icarus*, 220(2), 348–368. <https://doi.org/10.1016/j.icarus.2012.05.022>
- Villarreal, M. N., Russell, C. T., Luhmann, J. G., Thompson, W. T., Prettyman, T. H., A'Hearn, M. F., et al. (2017). The dependence of the Cerean exosphere on solar energetic particle events. *The Astrophysical Journal Letters*, 838(1). <https://doi.org/10.3847/2041-8213/aa66cd>
- Viola, D., McEwen, A. S., Dundas, C. M., & Byrne, S. (2015). Expanded secondary craters in the Arcadia Planitia region, Mars: Evidence for tens of Myr-old shallow subsurface ice. *Icarus*, 248, 190–204. <https://doi.org/10.1016/j.icarus.2014.10.032>
- White, O. L., Schenk, P. M., Bellagamba, A., Grimm, A., Dombard, A. J., & Bray, V. (2017). Impact crater relaxation on *Dione* and *Tethys* and relation to past heat flow. *Icarus*, 288, 27–52.
- White, O. L., Schenk, P. M., & Dombard, A. J. (2013). Impact basin relaxation on Rhea and Iapetus and relation to past heat flow. *Icarus*, 233, 699–709.
- Williams, D. A., Buczkowski, D. L., Mest, S. C., Scully, J. E. C., Platz, T., & Kneissl, T. (2017). Introduction: The geologic mapping of Ceres. *Icarus*, 316, 1–13. <https://doi.org/10.1016/j.icarus.2017.05.004>
- Williams, N., Bell, J., Christiansen, P., & Farmer, J. (2014). Evidence for an explosive origin for central pit craters on Mars, Eight Intl. Conf. on Mars, 1041.
- Wood, C. A., Head, J., & Cintala, M. (1978). Interior morphology of fresh Martian craters—The effects of target characteristics, Proc. Lunar Plan. Sci. Conf. IX, 3691-3709.
- Yasuda, K., & Ohmura, R. (2008). Phase equilibrium for clathrate hydrates formed with methane, ethane, propane or carbon dioxide at temperatures below the freezing point of water. *Journal of Chemical & Engineering Data*, 53(9), 2182–2188. <https://doi.org/10.1021/je800396v>